EXPERIMENTAL STUDIES OF PARTICLE PRODUCTION IN ULTRA-RELATIVISTIC HEAVY ION COLLISIONS

PÅL NILSSON

DIVISION OF COSMIC AND SUBATOMIC PHYSICS
DEPARTMENT OF PHYSICS
LUND UNIVERSITY, SWEDEN

THESIS FOR THE DEGREE OF DOCTOR OF PHILOSOPHY

FACULTY OPPONENT: PROF. RAINER RENFORDT

TO BE PRESENTED UNDER THE AUSPICES OF THE FACULTY OF MATHEMATICS AND NATURAL SCIENCES OF LUND UNIVERSITY AND PUBLICLY DEFENDED IN LECTURE HALL B OF THE DEPARTMENT OF PHYSICS ON OCTOBER 5 2001, AT 10.15.

Organization **LUND UNIVERSITY** Department of Physics Box 118 SE-221 00 LUND, Sweden	**Document Name** **DOCTORAL DISSERTATION** **Date of issue** 1 September 2001 **CODEN:** ISRN LUNFD6/NFFK--2001--1019-SE-140P
Author(s) Pål Nilsson	**Sponsoring organization**

Title and subtitle

Experimental studies of particle production in ultra-relativistic heavy ion collisions

Abstract

This thesis is about high energy heavy ion physics. Two major experiments, the WA98 at CERN and the PHENIX at Brookhaven National Laboratory, are described. Results from data analysis from both experiments are presented.

The WA98 chapter presents particle identification methods and phi-meson measurements. A procedure for calculating efficiency maps for tracking chambers is discussed.

The PHENIX chapter gives a technical overview of the Pad Chamber reconstruction software and ends with an analysis of single particle spectra based on 65+65 A GeV Au+Au data.

The thesis is based on five papers. The first four describe the development of measurement and analysis methods, while the last paper was the first physics paper from the PHENIX experiment and is about charged particle multiplicity.

Key words

Pad chambers, pad readout, PHENIX, WA98, phi-meson, tracking, single particle spectra, heavy-ion collisions, inverse slope parameters, particle production, charged particle multiplicity, RHIC, SPS

Classification system and/or index terms (if any)

Supplementary bibliographical information	**Language** English
ISSN and key title 1101-4202 Cosmic and Subatomic Physics Dissertation	**ISBN** 91-7874-141-6

Recipient's notes	**Number of pages** 196	**Price**
	Security classification	

Distribution by (name and address)

Pål Nilsson, Department of Physics,
Box 118, SE-221 00 LUND, Sweden

I, the undersigned, being the copyright owner of the abstract of the above-mentioned dissertation, hereby grant to all reference sources the permission to publish and disseminate the abstract of the above-mentioned dissertation.

Signature Pål Nilsson **Date** August 27, 2001

Populärvetenskaplig sammanfattning (Popularised summary in Swedish)

Denna lilla skrift behandlar ett område inom fysiken som kallas högenergetisk tungjonsfysik. Kort förklarat betyder detta att vi studerar kärnmateria under extrema förhållanden, såsom höga temperaturer och höga tryck. För att åstadkomma dessa, kolliderar vi bly- och guldkärnor med mycket höga energier vid partikelacceleratorer, i USA (New York) och i Schweiz (Genève). När kärnorna kolliderar smälter dessa till en soppa av sina innersta beståndsdelar, kvarkar och gluoner. Är energin tillräckligt hög hoppas vi kunna skapa ett s.k. kvark-gluon plasma, där kvarkarna och gluonerna uppträder som fria partiklar, om än för en kort stund; en miljarddels miljarddels sekund eller så. Man säger att en fasövergång har ägt rum, ungefär som då kokande vatten övergår i vattenånga. Liknande när vattenångan kondenserar tillbaka till flytande form då den kyls av, kommer kvark-gluon plasmat att kondensera till kärnpartiklar, såsom protoner och neutroner men även andra mer exotiska partiklar som pioner och kaoner. Detta studium visar sig även vara viktigt för vår förståelse av universums tidiga utveckling. Fram till en miljondels sekund efter Big Bang (den stora smällen), bestod universum av ett kvark-gluon plasma som snabbt expanderade. I våra experiment försöker vi återskapa de förhållanden som rådde i universum när det var ungt. För att göra detta har vi konstruerat detektorer, stora som flervåningshus, för att kunna registrera de ytterst små partiklarna. Denna avhandling beskriver bl.a. utvecklingen av mätinstrument, metoder, och hur informationen som kommer från detektorn tas om hand när den används i experimentet. Under experimentets gång genereras gigantiska datamängder, omkring 20MB i sekunden, som sedan analyseras. Avhandlingen innehåller även analys av sådan data, där en uppskattning görs av partikeltätheten och temperaturen hos kärnmaterien skapad i guld-guldkollisioner, vid tio gånger högre energi än tidigare.

Avhandlingen är indelad i fem kapitel, utöver de fem artiklar som avhandlingsarbetet har resulterat i. Första kapitlet är en introduktion till ämnesområdet riktat till icke experter. Den käre läsaren ledsagas genom universums historia som vi känner den, till hur vi studerar Big Bang i laboratoriet. De senare delarna är av mer teknisk natur, där andra kapitlet behandlar WA98 experimentet som kördes på CERN i Schweiz under flera år fram till senhösten 1996. Tredje kapitlet avhandlar PHENIX experimentet på Brookhaven National Laboratory i USA, medan det fjärde innehåller en sammanställning av vad vi har lärt oss vad gäller de mer tekniska delarna av avhandlingen. Sista kapitlet är en kort sammanfattning av artiklarna som återfinns i sin helhet i appendix I-V.

Pål Nilsson
Lund, 27:e augusti, 2001.

This thesis is based on the following publications:

- I **A large-acceptance spectrometer for tracking in a high multiplicity environment, based on space point measurements and high resolution time-of-flight**
  Nucl. Instr. and Methods **A** *431 (1999) 123-133.*
  L. Carlén et al.

- II **The pixel readout system for the PHENIX pad chambers**
  Nucl. Phys. **A** *661 (1999) 665c-668c.*
  P. Nilsson.

- III **Event reconstruction in the PHENIX central arm spectrometers**
  Accepted for publication in Nucl. Instr. and Methods.
  J. T. Mitchell et al.

- IV **Construction and performance of the PHENIX pad chambers**
  To be submitted to Nucl. Instr. and Methods.
  K. Adcox et al.

- V **Centrality dependence of charged particle multiplicity in Au+Au collisions at $\sqrt{s_{NN}} = 130$ A GeV**
  Phys. Rev. Lett. **86** *(2001) 3500-3505.*
  K. Adcox et al.
  Copyright 2001 by the American Physical Society.

All published papers are reprinted with the permission of the copyright holders,

Elsevier Science Publishers B.V. P.O. Box 103 1000 AC Amsterdam The Netherlands	American Physical Society One Physics Ellipse College Park MD 20740-3844 U.S.A.

The cooperation of the copyright holders is gratefully acknowledged.

Acknowledgments

I have many people to thank for this thesis, which would not have been written without their kind help. When I started my master thesis work in 1996, Prof. Ingvar Otterlund was very encouraging and introduced me to this rich field of science. I stayed in the high-energy group for my Ph.D. work under the guidance of Dr. Anders Oskarsson (supervisor), Prof. Evert Stenlund and Dr. Sten Garpman (assisting supervisors). I am very grateful for their patience and for always having time to answer tricky questions. Same goes for the group leader, Prof. Hans-Åke Gustafsson, who also seem to have an unlimited supply of knowledge and good advice, not to mention the fact that he knows everyone in this business, which can be quite practical sometimes. Dr. Joakim Nystrand, Dr. Lars Carlén and Lennart Österman for likewise providing kind help. Dr. Vladimir Avdeichikov for being my kind neighbour. Our secretary, Bozena Wlosinska, for sorting out all my complicated traveling expenses, etc. All the students over the years, Dr. Tom Svensson, Dr. Karim El Chenawi, Dr. Johan Mårtensson, Dr. Anton Fokin, Dr. Roberta Ghetti, Lic. David Silvermyr, Lic. Corina Andreoiu, Lic. Milena Mineva, Pavel Golubev, Henrik Tydesjö, Rickard du Rietz and Jörgen Ekman for creating a really good atmosphere at the division; especially David and Karim whom I owe a lot!

Dr. Jeffery Mitchell (BNL[1]), Prof. Charles Maguire (VU[2]), Dr. Indrani Ojha (VU) for providing lots of software help over the years.

Dr. Hans-Uno Bengtsson for fruitful comments on the cosmology section. Dr. Per-Olof Zetterberg for letting me teach the undergraduate students. Last but not least, Dr. Peter Ekström and Dr. Tomas Brage for hiring me to work on the information project at the Department of Physics[3].

I gratefully acknowledge the financial support from Kungliga Fysiografiska Sällskapet i Lund, Knut och Alice Wallenbergs Stiftelse and Jacob Letterstedt's Stipendiefond.

---

[1] Brookhaven National Laboratory, New York, USA.

[2] Vanderbilt University, Tennessee, USA.

[3] See http://fysik.lu.se and http://fysikilund.lu.se

To my mother and
the memory of my father

Contents

Paper III

Paper IV

Paper V

Chapter 1

Introduction

> "If it were possible to experiment with neutrons or protons of energies above a hundred million volts, several charged or uncharged particles would eventually leave the nucleus or as a result of the encounter; with particles of energies of about a thousand of million of volts, we must even be prepared for the collision to lead to an explosion of the whole nucleus."
>
> - Niels Bohr, Nature 137(1936)351.

What once was only dreamed about, in the minds of giants, is now possible at several facilities around the world. At CERN in Switzerland and at Brookhaven National Laboratory (BNL) in the United States, nuclei from heavy atoms are accelerated to extremely high energies colliding with a fixed target or to a beam of nuclei coming from the opposite direction. When two such ions collide, literally thousands of particles are created, flying out of the collision zone together with the remnants of the incoming nuclei.

As it turns out, these studies are important for understanding the origin of our universe. The small can be seen in the large, and the large in the small. In the following pages, two major experiments are described that were built for exploring the universe within the atom.

1.1 The history of the universe

The creation of the universe took place some 12-15 billion (10^9) years ago. At the very first instant of the newly born universe, it is believed that all forces of nature were united in a single force. After 10^{-43} seconds, the gravitational force was suddenly decoupled, space-time became four-dimensional and the era of super unification ended. The era of grand unification began. The physics of this epoch is far from certain, but is believed to be described by a grand unified theory. The mediators of this force are the X, $\overline{X}$, Y and $\overline{Y}$ particles. Together with quarks, leptons and exchange particles they populated the universe. At the end of this epoch, the X and Y, as well as their anti-particles, disappeared from the universe. As they decayed, they left behind a small excess of quarks over anti-quarks with the ratio of $(10^9 + 1) : 10^9$.

When the universe was about 10^{-34} seconds old, it was blown up well beyond the observable edge of the universe. Despite this enormous expansion, the epoch of inflation was very short. At 10^{-33} seconds, it was over and the expansion settled into its "normal" rate. It has, however, recently been discovered from studies of distant supernovae that the expansion is slowly accelerating [1, 2, 3], implying a possible existence of a repulsive component in the gravitational force.

In the primordial fireball, the average energy per particle exceeded 10^{19} GeV [1] and most of it was in the form of radiation. As the universe continued to expand, it gradually cooled off.

Up until 10^{-10} seconds, when the average energy had sunk to around 100 GeV, the particle soup also contained W and Z-bosons in thermal equilibrium. Quarks and anti-quarks were too close to each other for the strong force to bind them into hadrons. Any system that was temporarily bound together, would immediately be

---

[1] Being the original seed of our universe, a quantum bubble the size of Planck length dimensions, $l_P = ct_P = \sqrt{\frac{\hbar G}{c^3}}$, had an energy density of $\rho_P = \frac{m_P}{l_P^3}$ where the Planck mass is given by $m_P = \sqrt{\frac{\hbar c}{G}}$. The energy can then be calculated from $E = m_P c^2 = \rho_P l_P^3 c^2$.

blasted apart by the high energy particles that also were present. Also mixed up in this soup were the mediators of the strong force, the gluons, which together with the quarks are often referred to as partons.

The free state of partons, called a *quark-gluon plasma* (QGP), lasted until the first few microseconds had passed [4]. At this time it is believed that a phase transition took place which imprisoned the once free quarks and gluons into the particles we now call hadrons. In particular, protons and neutrons were formed.

As the temperature dropped below the threshold for proton and neutron production, virtually all anti-matter was removed from the universe leaving a small excess of matter behind. After the annihilation, there was one proton for every 10^9 photons. The surviving protons and neutrons were kept in thermal equilibrium with the rest of the universe via neutrino interactions. This lasted until one second after the Big Bang when the density became too low for maintaining the equilibrium. The neutrinos decoupled from the rest of the universe which, for the neutrinos, was transformed into a thin fog, barely observable.

When the universe was three seconds old, the remaining anti-matter in the form of positrons was removed by the excess of electrons. Three minutes later, the nucleosynthesis started and the first compound nuclei, deuterons, were formed by protons and neutrons. The deuterons quickly formed the helium nuclei ^{3}He and ^{4}He. Nucleosynthesis was halted some 13 minutes after the Big Bang, when the temperature had dropped below that required for nuclear fusion reactions.

After some 300 000 years, the average photon energy was not sufficient any more to prevent electrons from being captured by protons. The first atoms were formed. When this happened, the large number of free electrical charges disappeared. The photons had nothing to interact with and thus decoupled from matter. The universe became transparent. At approximately the same time, the radiation density dropped below the density of matter. The radiation era was over and the matter era began.

The first galaxies were not born until a billion years had passed.

The actual dynamics are not known. Huge clouds of gas and dust contracted to form stars, in which nucleosynthesis restarted and produced heavier elements. Solar winds swept through the local systems and removed most of the debris. Smaller lumps of matter became planets on which life itself was finally formed. From a simple molecule in a puddle of water, plants, fish and complex beasts with growing intelligence evolved. Eventually man was created, declared himself the crown of creation and began to speculate about his origin.

At this point in the history of the universe we are capable of reconstructing the conditions of the early universe, although on a much more modest scale. This is where our story begins.

1.2 The Big Bang in the laboratory

Looking deeply into matter, require probes of high energy. Until the 1950's, the only source of such probes was cosmic rays. These can be extremely energetic, but since the rate is low it makes statistical analysis difficult. Today, the overwhelming majority of experiments use large machines, known as accelerators, to produce beams of particles or nuclei.

1.2.1 Accelerators

There are different kinds of accelerators in use today. Relevant for this thesis are the fixed-target and the colliding-beam machines. In a fixed-target machine, the particles or ions are accelerated to the desired operating energy after which the beam is extracted from the machine and steered on to a stationary target. In colliding-beam accelerators, two beams coming from opposing directions are made to collide with each other. An advantage of using a collider is that all of the beam energy is available for particle production, in contrast to a single beam accelerator where a large fraction of the

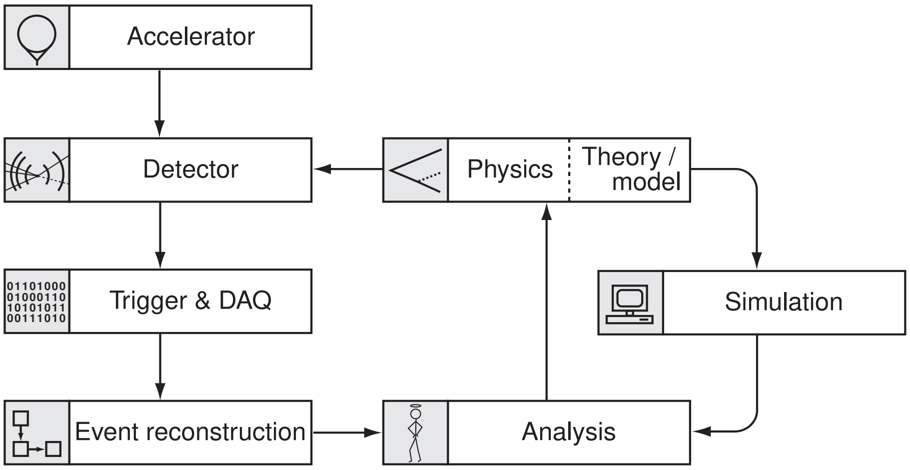

Figure 1.1: *The various steps of a physics experiment.*

energy is consumed by moving the center-of-mass frame. A disadvantage is however that the collision rate in a heavy ion collider is usually smaller than can be achieved with a fixed target.

An example of an accelerator for fixed-target experiments is the Super Proton Synchrotron (SPS), at CERN. It started as a proton accelerator but was later upgraded for acceleration of the nuclei ^{16}O and ^{32}S, with center-of-mass energy $\sqrt{s} = 19.4$ A GeV, and ^{208}Pb with $\sqrt{s} = 17.4$ A GeV.

In the summer of 2000, the Relativistic Heavy Ion Collider (RHIC) at BNL started to deliver ^{197}Au beams. The beams can each be accelerated up to 100 A GeV, which gives a center-of-mass energy of 200 A GeV. It was initially run at a beam energy of 65 A GeV.

With a startup in 2007, the Large Hadron Collider (LHC) at CERN will deliver Pb beams with a maximum center-of-mass energy of about 5 500 A GeV.

1.2.2 Experiments and detectors

The collisions leading to particle production take place on several stations (experiments) around the accelerator. In order to deduce details of the produced particles and eventually gain further knowledge of the laws of nature, each experiment has a set of devices known as detectors placed around a collision region. The detectors contain volumes of certain materials that are easily ionized by the traversing particles. The ionization is recorded by amplifying electronics for later hit reconstruction and analysis.

In a collision we have to track and identify the out coming debris as well as to understand exactly how it was created. For this purpose, very advanced detector systems have to be utilized. Two such systems, the WA98 and the PHENIX experiments, will be discussed in this thesis. Common to both of these experiments is the desire to study nuclear matter under extreme conditions such as high temperature and high pressure.

1.2.3 Experimental challenges

Heavy ion collisions present additional experimental difficulties compared to *pp*-collisions since the particle multiplicities are several orders of magnitude higher. Any detection aiming at observing individual particles must increase the granularity of the detector accordingly. Many of the interactions of the particles with the detector material have very small spatial extension and the appropriate granularity can be achieved by making the readout more granular. This is the case for e.g. gaseous ionization detectors which we deal with in this thesis. If the physical dimension is large, e.g. an electromagnetic shower, the granularity can only be achieved by moving the detectors out to a suitable distance (like the LEDA in WA98, see chapter 2) and increase the number of channels.

1.2.4 Detector construction

Although there are many different kinds of detectors, most of them are based on the principle of ionization. An obvious choice of a suitable detector medium is a gas, because of its great mobility of electrons and ions. When a charged particle traverses a gaseous volume it will ionize the gas. If an electric field is established, it will accelerate the positively charged gas atoms towards the cathode plane and the electrons towards the positive anode. If the electric field is strong, the accelerated electrons can ionize gas atoms resulting in an avalanche process which gives an amplification.

In a multi-wire proportional chamber (MWPC), the anode consists of many thin and closely spaced wires. The strong field is created by the fact that $E \sim \frac{1}{r}$, resulting in a very high E in the vicinity of the wire. It is possible to either read out the wires directly, or to divide the cathode plane into small electrodes (pads) and read out these instead. This has several advantages over wire readout; the most important being the removal of ambiguous signals caused by more than one particle passing close to the same wire.

The Pad Chambers in the PHENIX experiments are MWPC:s read out on finely segmented pad planes. It has partly been the responsibility of the Lund group to develop and fund these chambers, as well as their readout systems and analysis tools.

In the Multi-Step Avalanche Chamber (MSAC), used in the WA98 experiment, a homogeneous E-field is created by successive parallel meshes. The cloud of electrons liberated by the avalanches can be collected on the anode side of the chamber.

Thorough details about the PHENIX Pad Chamber construction can be found in Paper IV in this thesis, while the MSAC:s in the WA98 experiment are described in paper I.

1.2.5 Electronic readout

As mentioned, the granularity problem in gas chambers is reduced to finding a suitable electronic readout. In a typical central collision at RHIC, thousands of particles traverse the detector system. This generates a tremendous amount of data from the sub system electronics that need to be taken care of before the next collision takes place on the average a few hundred microseconds later. Events are buffered to cope with fluctuations in the event rate. In the PHENIX experiment, the data rate at full luminosity is about 20 MB/s. In the future ALICE experiment at the LHC, the rate is expected to be about 1.2 GB/s. Since the total time of data collection is on the order of several years, this puts extreme demands on storage systems and processors, not to mention the programmers that need to write fast code.

Due to the immense number of particles traversing the chambers, the readout electronics must have many readout channels in order to resolve the tracks. Since the signals from the sensing electrodes are very small and thus won't survive undisturbed any longer trace distances, it is often a requirement that the readout electronics are mounted on the chamber, in the path of the traversing particles. This in turn means that the electronics must be made very thin, in order not to disturb the particles passing through.

The many channels can potentially be very expensive, both in cost and power consumption. The concepts presented in this thesis (papers II and IV) describe a readout system that reduces this cost drastically. By introducing a simple readout channel, close to the pad that has a complex structure made to reduce the number of channels, we achieve low cost, high performance, low power and minimal data volume. The minimal material thickness is achieved by realizing the front-end amplifying and digitizing electronics in specially designed integrated circuits mounted with the chip-on-board technique on ultra-thin printed circuit boards.

1.2.6 Event reconstruction

The raw data coming from the detectors, or sub systems, is orders of magnitudes larger than the numbers given above. Most of this data is not worth saving and is thus removed by the hardware in the

Data Acquisition system (DAQ). Special triggers select the events that are considered to contain interesting data. The level-one triggers select events that are considered to be real events not triggered by cosmic radiation or other background signals, while the level-two trigger algorithms have been written to select special events, such as coherent peripheral collisions, events containing a detected J/ψ candidate, etc.

In the PHENIX experiment, the event data is stored in PRDF (PHENIX Raw Data Format) files. The selected events are processed by the reconstruction algorithms. These are described in detail for the WA98 and PHENIX experiments in papers I and III in this thesis. The reconstructed events are stored in DST (Data Summary Tape) files for later analysis. A typical DST file is quite large and usually contain more information than necessary for a certain analysis. They are thus often compressed into much smaller μDST files that are more easy to analyze, e.g. in the PAW [5] or ROOT [6] environments.

Analysis will eventually lead to physics results that either can be understood with existing theoretical models or to improve them. Theory and models form the basis of simulation. The entire experiment can be simulated by software using input from event generators, such as Fritiof [7], RQMD [8], HIJING [9], NEXUS [10] etc. The GEANT tool [11] was developed for this purpose and is heavily used in the particle physics community, but also in other areas of science. With this tool, the detectors are first modeled in 3D. Functions are then added to simulate the response of the modeled detectors. When the simulation is run, the input data from an event generator, i.e. the generated particles, are stepped through the detector system. The output file is ideally of the same format as real data in order to read it seamlessly into the same analysis package.

1.2.7 Analysis

Before the physics analysis can begin, enough statistics (data) has to be collected. In addition to this, the response of the detector subsystems must be understood and the cuts that should be applied to the data in order to remove background etc need to be investigated. Normally, a detector system can not record all emitted particles. This limitation, called the detector acceptance, can be due to geometrical coverage and/or limitations in momentum outside of which particles may not enter the detector (low momentum) or may not be identified (high momentum). When these things are understood by simulation, the corrections can be determined, the raw spectra can be produced and the physics analysis can start.

1.3 The quark-gluon plasma

If hadrons were subjected to the same energy densities as the state of the universe during the first microsecond, one would recreate the conditions of the early universe in a system of nuclear size and generate a phase transition back to the free parton state. Assuming that this is indeed possible, how would we know that a phase transition really took place? It is generally recognized that there is no single unique signal to look for that guarantees that a QGP has been formed. What can be achieved may be a set of signals that, when taken together, may indicate the presence of the deconfined state. A few such probes will now be discussed briefly.

1.3.1 Thermodynamical variables

A phase transition can be classified according to the discontinuity of the free energy F as a function of the temperature T [12]. The phase transition is said to be of the nth order if the nth partial derivate $\partial F/\partial T$ is discontinuous while all the lower derivatives in

T are continuous. Since the free energy can be written

$$F = E - TS \tag{1.1}$$

where E is the internal (total) energy and S is the entropy, we have that

$$S = -(\frac{\partial F}{\partial T})_E \tag{1.2}$$

According to the definition above, a first order phase transition is thus characterized by a discontinuous entropy and a continuous free energy as a function of temperature. An example of a first order phase transition is the liquid to gas process of boiling water.

In a system of colliding nuclei, the particle density ($dN/d\eta$) can be related to the entropy [13]. Furthermore, it is usually assumed that a measure of the system temperature can be obtained from the $< p_T >$ or the exponential slope of the p_T-distribution of the produced particles. During the collision process, the system will be heated until it reaches a critical temperature, T_c. At this point the system remains in a mixed state at a constant temperature until the phase transition is complete. A first order phase transition should therefore be seen in a $< p_T >$ versus $dN/d\eta$ plot as a plateau and a rise. T_c could then be determined from the $< p_T >$ at the level of the plateau.

Another interesting variable is the energy density, ϵ, which can be derived from Eq. 1.1 above by dividing the total energy with the volume,

$$\epsilon = \frac{E}{V} = \frac{F + TS}{V} \tag{1.3}$$

It is experimentally most commonly estimated from the Bjorken formula [14]

$$\epsilon_{Bj} = \frac{1}{\pi R_0^2 c\tau_0}\frac{dE_T}{d\eta} \tag{1.4}$$

where E_T is the transverse energy, R_0 is the transverse radius of the system and τ_0 is the formation time, usually taken as 1 fm/c.

1.3.2 Strangeness enhancement

As predicted by Rafelski et al. [15] and later confirmed by lattice QCD calculations [16], the strangeness content in a quark-gluon plasma in thermal and chemical equilibrium is believed to be enhanced from that of normal hadronic matter. The strange quark production is expected to be enhanced since the up and down quarks are Pauli blocked due to their high concentration and to the high Fermi energy they would have to overcome. The creation of $s\overline{s}$ pairs might therefore be energetically favourable over the creation of $u\overline{u}$ or $d\overline{d}$ pairs, if the available energy is above $2m_s\mathrm{c}^2$. In a gluon rich plasma, the strange quark pairs will predominantly be produced by gluon-gluon interactions. The estimated equilibration time is of the order of a few fm/c, i.e. of the same order as the interaction time of a high energy heavy ion collision.

An enhancement in the strangeness production can also happen in a hot and dense hadronic gas. The relative abundance of strange particles in that scenario could gradually grow in a chain of rescattering processes. In this case however, the characteristic time scale is on the order of 100 fm/c, i.e. much longer.

It should be pointed out that any observed strangeness, whether it originates from a QGP or not, is a powerful probe of the reaction dynamics as there is no strangeness in the initial state. All strange hadrons are created in the interaction.

The enhancement should be more pronounced for multi-strange hadrons, e.g. ϕ-mesons ($s\overline{s}$) and Ω-baryons (sss), than for singly strange hadrons, like the K-mesons ($K^+ = u\overline{s}$, $K^0 = d\overline{s}$, $\overline{K_0} = \overline{d}s$, $K^- = \overline{u}s$). To avoid ambiguities, it would be even better to study anti-hyperons (e.g. $\overline{\Lambda}$) since they are not likely to be produced by hadronic rescattering.

Several experiments at the AGS (BNL) and SPS (CERN) have observed strangeness enhancement. At AGS energies (14.6 A GeV) it was first observed by the E802 experiment in Si-induced central collisions as an increase in the K^+/π^+ ratio [17]. At 158 A GeV/c $Pb + Pb$ collisions at the SPS, WA97 has reported a large excess for particles of higher strangeness content, as compared to $p + A$. For $\Omega^- + \overline{\Omega}^+$ the factor is about 20 [18].

1.3.3 Light vector mesons

It has been suggested (e.g. in [19]) that the mass, width, branching ratios and yields of light vector mesons (such as ρ, ω and ϕ) differ from normal nuclear matter when produced in hot, dense and strongly interacting matter. E.g. the branching ratios between

$$\phi \rightarrow \begin{cases} K^+ + K^- & (49.1 \pm 0.8)\% \\ e^+ + e^- & (2.99 \pm 0.08) \times 10^{-4}\% \end{cases} \tag{1.5}$$

are very sensitive to mass changes. If chiral symmetry is restored, which it is believed to be inside a plasma [20, 21], the quark masses go to zero. Since the mass of the ϕ-meson is very close to twice the kaon mass, $m_\phi - 2m_K = 32$ MeV/c^2, and the kaon channel is the dominant decay mode, the ϕ decay will be highly susceptible to changes in the strange quark mass. The kaon decay mode would be prohibited and the branching ratios between the kaon and electron channel be modified.

The PHENIX experiment at RHIC will measure both of these channels, while the NA49 [22] and WA98 experiments (see section 2.5) at the CERN SPS have measured the $K^+ + K^-$ channel.

1.3.4 Direct photons

Photons created in the collision do not interact strongly with the plasma and can thus escape from the hot zone carrying information about the early stages of the interaction. Since the production rate and momentum distribution of these direct photons, also known as thermal photons, are determined by the momentum distributions of the quarks and gluons, they can give information about the thermodynamical state of the environment in which they are produced. However, it is not a trivial task to distinguish the direct photons from the photons coming from other sources such as $\pi^+ + \pi^- \rightarrow \gamma + \rho_0$. A copious source of photons come from hadronic decay, e.g. abundantly produced neutral mesons that decay into photon pairs forming an experimental background.

The WA98 experiment has published results constituting the first observation of direct photons in ultra-relativistic heavy-ion collisions [23].

1.3.5 J/ψ suppression

The J/ψ particle is the bound state of a charm and anti-charm quark. It has been suggested that the production of this resonance will be suppressed in a QGP due to Debye screening of the color charges [24]. It will thus be more probable for the $c(\overline{c})$ to combine with one of the more abundant $\overline{u}(u)$ or $\overline{d}(d)$ quarks in the hadronization process to form a D-meson rather than a $\overline{c}(c)$ to form a J/ψ.

A suppression has indeed been observed when going from lighter $(p + U)$ to heavier $(S + U)$ systems [25]. However, it has been shown that this is consistent with suppression due to absorption in a dense medium [26]. In heavier systems still $(Pb + Pb)$, the suppression has been found to be much stronger than what can be expected from an extrapolation from the lighter systems [27, 28, 29]. It is as of yet not clear whether this is due to the formation of a QGP or if it could be explained by other mechanisms.

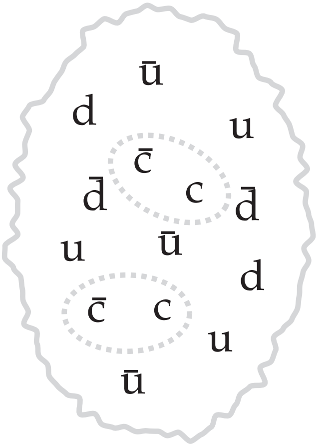

Figure 1.2: *Debye screening in a plasma.*

1.3.6 Neutron stars

Quark matter may not only be formed in particle physics facilities on earth, but also in the far reaches of space, deep inside the remnants of old and once massive stars.

It is a known fact that rotating neutron stars slow down with time due to interactions between the electromagnetic field and the surrounding matter. When the centrifugal forces become smaller, the pressure and density in the core region increase, and a phase transition of the first order may occur in the center. Glendenning et al. [30] found that a drastic softening of the equation of state, e.g. by a phase transition to a QGP, can lead to a rapid contraction of the neutron star at a critical angular velocity and that this will show up as a back bending moment of inertia as a function of frequency. As the star slows down, it will become unstable. The sudden decrease of inertia due to the dramatical changes in the core would create a large glitch which in principle could be observed by careful monitoring of young pulsars.

Chapter 2

The WA98 Experiment

This CERN SPS based, fixed-target experiment, was a large acceptance spectrometer for measurements of photons and hadrons in $^{208}Pb+^{208}Pb$ collisions at 158 A GeV. The aim was to study highly excited and compressed matter, and to search for possible quark-gluon plasma signals predominantly by the direct photon signals. The WA98 experiment ended its data taking in November 1996.

This chapter presents the experiment, a procedure for calculating efficiency maps for tracking chambers, as well as particle identification methods and ϕ-meson measurements.

2.1 Physics objectives

Since several of the suggested quark-gluon plasma signals were covered, the strategy was to measure both hadrons and photons and to study their correlations. Observables studied in this experiment are: charged particle and photon multiplicities, thermal photon emission, energy flow, single particle spectra, charged particle correlations and the production of hadronic resonances such as the Δ^{++} and the ϕ-meson.

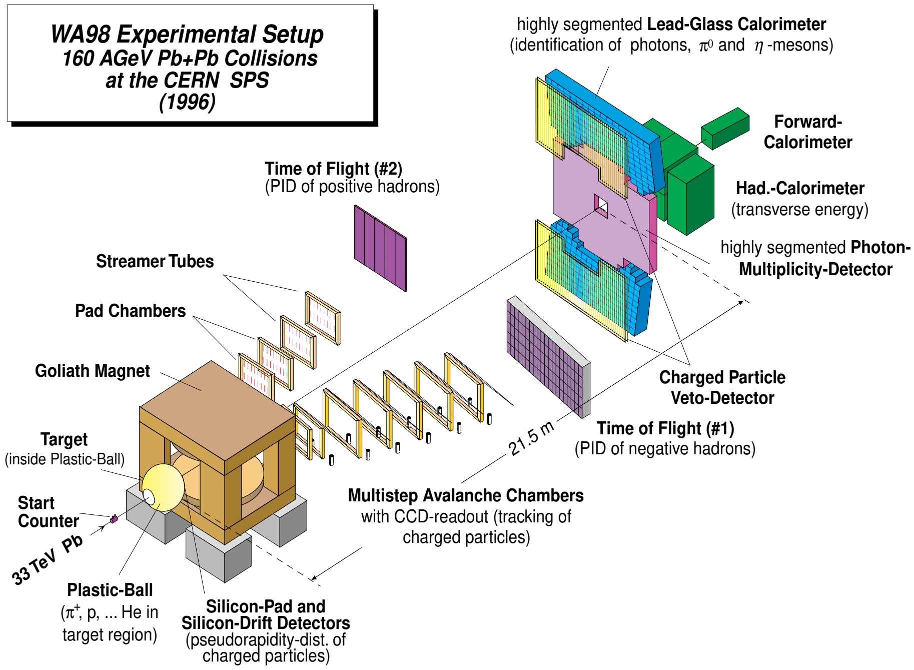

Figure 2.1: *The WA98 experimental setup for the 1996 Pb run.*

2.2 Experimental setup

The Beam Counter and veto detectors. The *Pb* beam provided by the CERN SPS, enters the experimental setup from the lower left in Fig. 2.1. Before it hits the target, it passes the nitrogen gas Čerenkov beam counter which provides a fast start signal for the time-of-flight measurements discussed below. The time resolution is about 30 ps. At a distance of 5.7 m upstream of the target, a halo detector was placed to reject interactions before the beam counter which in turn reject beam particles with charges different from that of the lead nucleus. At a distance of 2.7 m upstreams, a veto detector was placed to limit the beam profile for accepted collisions. A clean beam trigger was obtained by the beam counter in anti-coincidence with the inner halo and the veto detector.

The Plastic Ball. This detector system identified charged particles such as π^+, protons and light ions and was mainly used to determine the reaction plane of the collision [31]. The target during the 1996 Pb run was a 0.2 mm thick lead foil placed in the center of the Plastic Ball detector.

The Silicon Drift and the Silicon Pad Multiplicity Detectors. The multiplicity and pseudorapidity of charged particles were measured by the Silicon Drift Detector (SDD) and the Silicon Pad Multiplicity Detector (SPMD) [32], located 12.5 and 30 cm downstream of the target. The pseudorapidity range of the SDD was $2.0 < \eta < 3.4$, and $2.35 < \eta < 3.75$ for the SPMD.

The Goliath magnet. A magnetic field with a bending power of 1.6 Tm was provided by the Goliath magnet. The center of the magnet was located 3.28 m downstream of the target. The polarity of the field was such that negatively charged particles were bent into the first tracking arm (described in section 2.2.1 below), while positively charged particles were bent into the second tracking arm (section 2.2.2). During the 1996 run, the polarity of the field was reversed during shorter periods.

The Mid-Rapidity and the Zero Degree Calorimeters. The last part of the trigger system consists of the Mid-Rapidity Calorimeter (MIRAC) and the Zero Degree Calorimeter (ZDC). MIRAC provided a complete coverage of the transverse energy, E_T, over the forward pseudorapidity interval of $3.5 < \eta < 5.5$ and was used to estimate the energy density, ϵ_{Bj} as well as to provide the centrality trigger. The remnants of the projectile was measured by the ZDC at angles less than $0.3°$ to the beam.

The Lead Glass Calorimeter. The Lead Glass Calorimeter or the Lead glass Detector Array (LEDA) was designed to detect thermal photons [33]. It consisted of 10 080 lead-glass modules each with a size of $4{\times}4{\times}40$ cm^3 and had a good energy resolution as well as fine granularity needed for a high resolution and a high reconstruction efficiency. The LEDA was placed 21.5 m downstream of the target, covering a pseudorapidity range of $2.28 < \eta < 2.95$ which corresponds to an angular range of $6° < \theta < 11.6°$.

The Charged Particle Veto Detector. In front of the LEDA, streamer tube detectors [34] equipped with pad readout were placed. Serving as charged particle veto detectors, it improved the photon reconstruction efficiency in the LEDA. Except for the pad size and tube length, these were of the same construction as the two planes of streamer tube detectors in the second tracking arm (described below).

The Photon Multiplicity Detector. Located 21.5 m from the target, the Photon Multiplicity Detector (PMD) [35] was a large and highly segmented pre-shower detector with a pseudorapidity coverage of $2.8 < \eta < 4.4$. It measured the photon multiplicity by conversion into electromagnetic showers in a 2 cm lead layer. The showers were detected by scintillator pads read out by CCD-cameras. Together with the SPMD, the PMD has been used to study fluctuations in the N_γ/N_{ch} ratio on an event-by-event basis, in the search for disoriented chiral condensates [36].

2.2.1 The first tracking arm

The first tracking arm consisted of six tracking planes followed by a time-of-flight wall used for the particle identification. During a normal run, the orientation of the magnetic field bent negatively charged particles into the first tracking arm.

The Multi-Step Avalanche Chambers. The gaseous Multi-Step Avalanche Chambers (MSAC:s) [37, 38, 39, 40] used as tracking planes, were equipped with an optical readout by CCD cameras. The chambers were located between 3.4 m and 9.4 m from the center of the Goliath magnet.

The Russian Time of Flight Wall. The time-of-flight wall, known as the RTOF, allowed particle identification of π^-, K^- and

$\overline{p}$. It was made of 480 plastic scintillators that were read out from both ends by photomultipliers. The time resolution was $\sigma_t = 120$ ps. It was located 13.5 m from the center of the magnet.

2.2.2 The second tracking arm

A second tracking arm was implemented in the experiment for the 1996 run, allowing the measurement of positively charged particles such as π^+, K^+ and p as well as the double charged Δ^{++} resonance [41] decaying into a π^+ and p. The combination of this arm with the first arm, rendered the possibility to reconstruct light vector mesons such as the ϕ-meson (see section 2.5).

The four tracking planes were two pad chambers (Fig. 2.2) and two streamer tube chambers (Fig. 2.3). Particle identification was achieved with a time-of-flight wall.

The development and construction of this tracking arm was the main contribution from the Lund group to the experiment in 1996. The chambers and their performance are described in more detail in paper I.

The Pad Chambers. The so-called pad chambers are in principle MSAC:s of the same type as in the first arm but are equipped with a pad readout [42, 43, 44] instead of CCD camera readout. The number of pads per chamber is approximately 36 000, each individually read out. The size of a pad is $1{\times}17$ mm^2. A hit is defined as two or more neighbouring pads that have received charge above a pedestal value. The pad layout is shown in Fig. 4.1.

The Streamer Tubes. The two streamer tube planes, located after the pad chambers, were also equipped with a pad readout. There are about 6 000 pads per plane with a size of $7{\times}22$ mm^2.

The Japanese Time of Flight Wall. The particle identification is done with a time-of-flight wall known as the JTOF and was constructed by the Japanese team. It consists of 480 slats of scintillators that are read out at both ends by phototubes. The

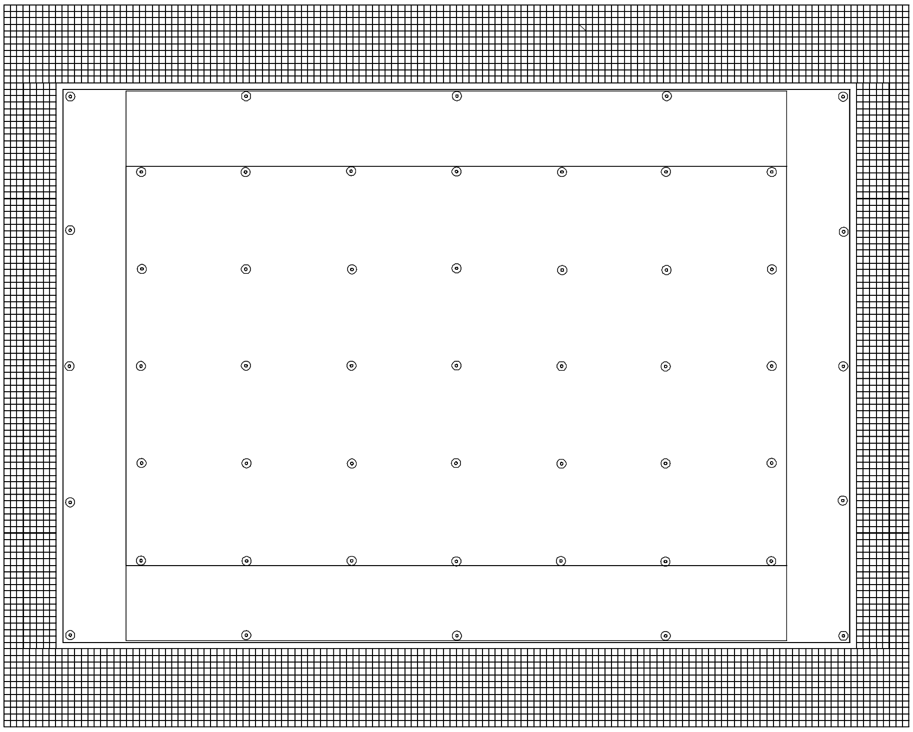

Figure 2.2: *A front view schematic picture of a Multi-Step Avalanche Chamber (MSAC).*

JTOF was constructed for the PHENIX experiment at RHIC and was used in the WA98 experiment for the first time.

2.3 Particle identification

Two different methods were utilized to identify pions, protons and kaons. For the first arm, the particles were separated in momentum-mass space (Fig. 2.4). Up to about 4 GeV/c in momentum, kaons are considered to be separated from pions. Anti-protons are not seen due to the limited statistics in the analysis described below

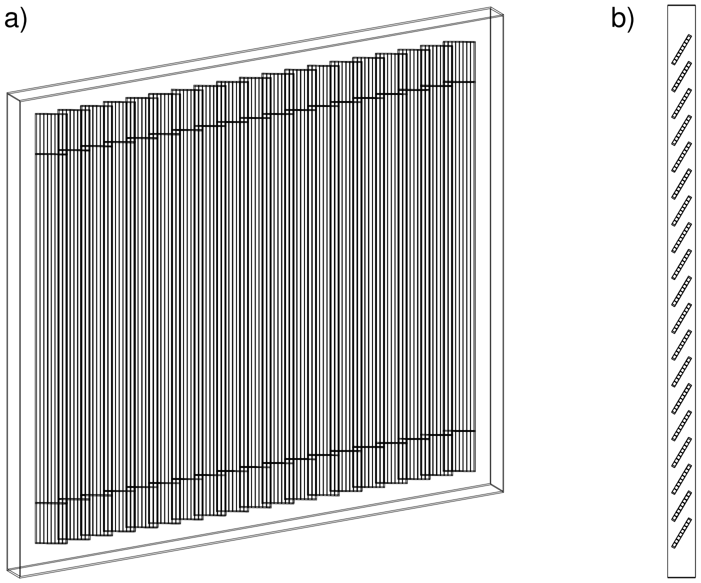

Figure 2.3: *A streamer tube chamber seen from a) behind and b) from above.*

(section 2.5). The separation of negative pions and kaons were done in a similar way to that described in chapter 3.5.2.

Another software method for particle identification is to compare the measured time-of-flight with the expected time-of-flight, assuming a given particle mass, and plot the momentum versus the time difference. This method was applied for the tracks in the second arm. Starting with the relativistic definition of momentum,

$$p = m_0 \beta c \gamma \tag{2.1}$$

the expected time-of-flight can be written as

$$t_{expected} = \frac{L}{c}\sqrt{1 + (\frac{m_0 c}{p})^2} \tag{2.2}$$

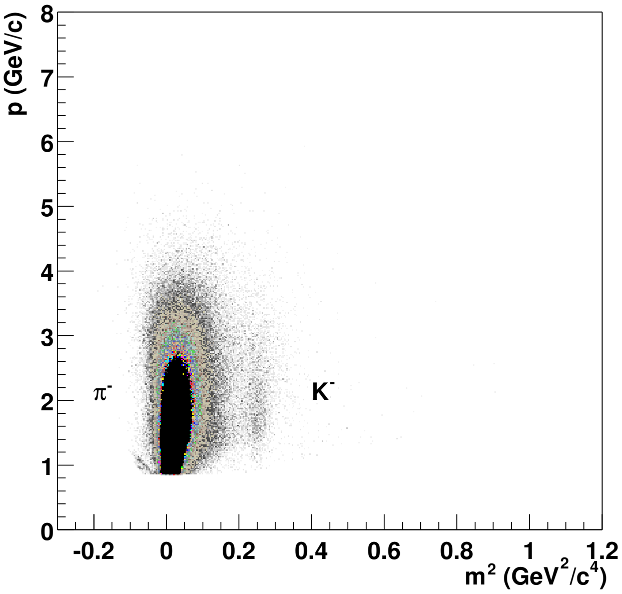

Figure 2.4: *Particle identification in the first tracking arm.*

where L is the actual flight path.

As is shown in Fig. 2.5, the various particles line up on narrow bands. By using this method, pions are more straightforward to separate from kaons.

2.3.1 Acceptance

Fig. 2.6 shows the acceptance of pions, kaons and protons in terms of transverse momentum (p_T) and rapidity (y). The transverse momentum is the projection of the momentum in the XY plane, where the plane normal vector is parallel to the beam line in our geometry. The p_T has been multiplied by the sign of p_x, which allows us to unfold low momentum particles that have bent over the beam line into the acceptance of the arm.

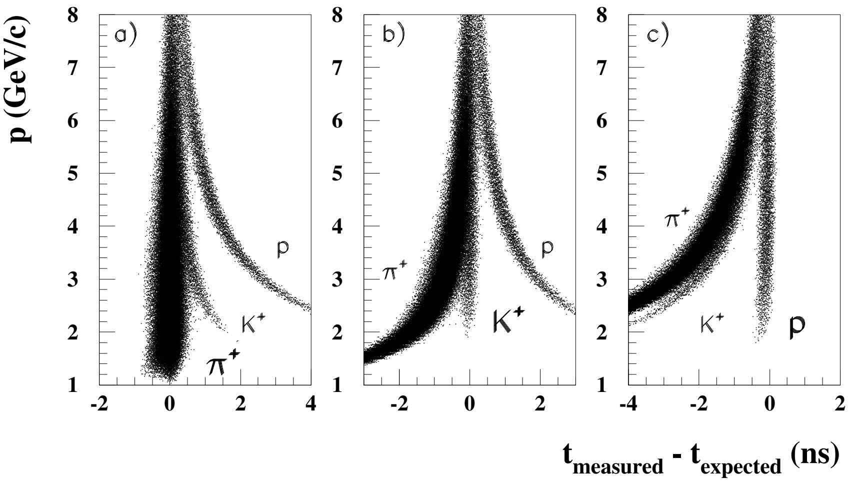

Figure 2.5: *Particle identification by assuming the mass of a a) pion, b) kaon and c) proton, used in the second tracking arm.*

2.4 Efficiency maps for the second tracking arm

The tracking efficiency for the pad chambers and the streamer tubes, was determined by projecting the tracks calculated from three chambers into the fourth chamber (same principle repeated for all chambers, see Fig. 2.7). The number of clusters ($N_{clusters}$) within a certain radius, corresponding to one or more hits, was then stored. A mixed event technique was used to determine the background. This was done by projecting the same track as before into the chamber in question, and search for clusters within the same radius but with cluster information from a different event. The number of found clusters, N_{mix}, was then subtracted from $N_{clusters}$. The resulting difference was stored in a two dimensional histogram at the coordinates of the projected hit. The ratio between this and the total number of projected hits in each bin gives the efficiency

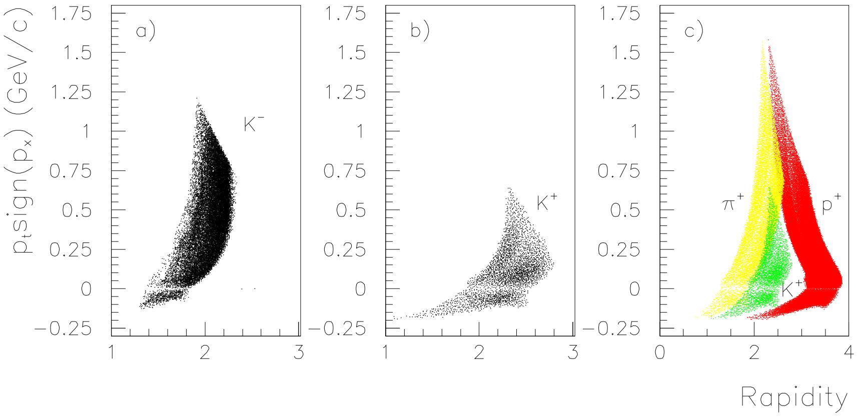

Figure 2.6: *The acceptance of kaons in terms of transverse momentum (p_T) and rapidity (y) for a) the first arm, and b) the second arm. c) Second arm acceptance of π^+, K^+ and p.*

map. The average efficiency as a function of radius was also studied. The tracks were projected to the target position, where the y-coordinate was calculated. Due to the finite size of the beam and the target, all tracks not coming from the target were rejected.

The χ^2-distributions for the tracks projected into the XZ- and YZ-planes were calculated with

$$\chi^2 = \frac{1}{N-n} \sum_{i=1}^{N} \frac{(y_i - y)^2}{\sigma_i^2} \tag{2.3}$$

where N is the number of chambers used in the fit (4), n being the number of fitting parameters (2), y_i is the coordinate Gaussian distributed around the mean y with a variance σ^2. The variances are set equal to the intrinsic chamber resolutions (see Table 2.1) folded with the effects of multiple scattering and a finite size of the target.

A cut was applied in both χ^2-distributions at $\chi^2 = 1.5$. The

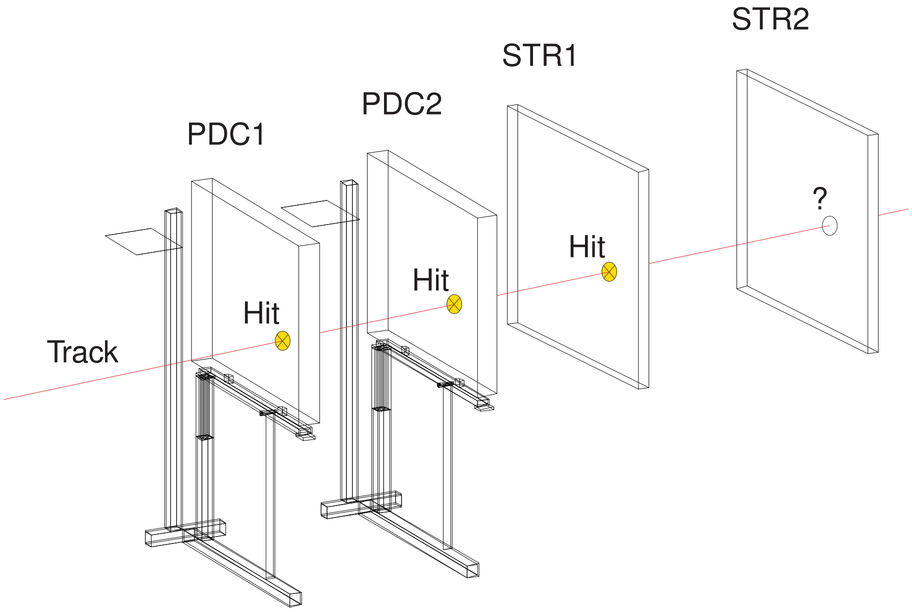

Figure 2.7: *A track fitted to clusters in the first three chambers. How many clusters can be found within a small radius in the fourth chamber?*

Table 2.1: The intrinsic and folded position resolutions in x and y for the second arm tracking chambers.

Chamber	*Intrinsic resolution (mm)*		*Folded resolution (mm)*	
PDC1	0.5	1.7	1.28	2.10
PDC2	0.5	1.7	1.26	2.25
STR1	3.0	6.5	2.61	6.95
STR2	3.0	6.5	4.66	7.71

limit was determined by comparing the χ^2-distribution to that of a theoretical χ^2 probability density function for N degrees of freedom

$$f(X) = \frac{\frac{1}{2}(\frac{X}{2})^{\frac{N}{2}-1}e^{-\frac{X}{2}}}{\Gamma(\frac{N}{2})} \tag{2.4}$$

Since the fit was done using three out of four chambers and with two fitting parameters, the number of degrees of freedom is one. The long tail in Fig. 2.8 is due to background. The cut was made where the background clearly dominated.

As can be seen in Fig. 2.9b and Fig. 2.10b, the average efficiencies level out at a radius of 11 mm for PDC1 and at 9 mm for PDC2. The average efficiencies have been corrected for the fuzzy borders where the fluctuations are larger due to limited statistics, as well as

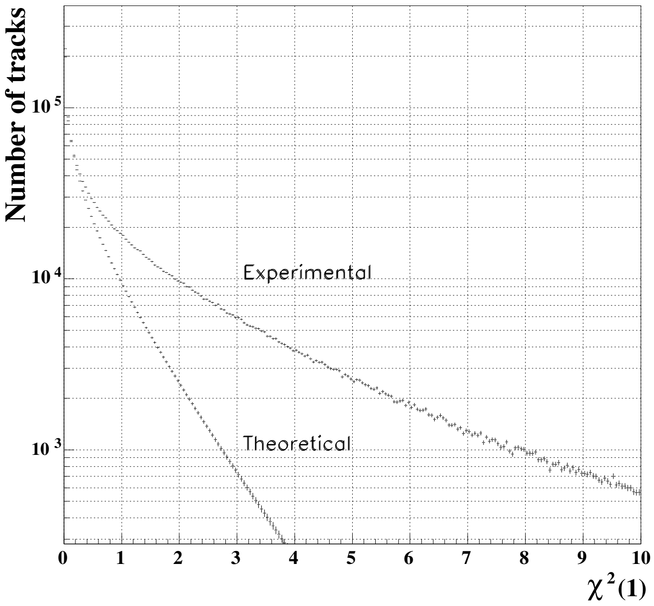

Figure 2.8: *The χ^2-distribution for the tracks projected onto the YZ-plane and the theoretical distribution normalized to the same number of tracks.*

for the dead areas in PDC2 clearly seen in Fig. 2.10a. The dead areas are due to a malfunctioning board module. The regular pattern of lower efficiency seen in both maps are due to the spacers located between the high voltage meshes in the chamber, stopping most electrons. The shadow seen in the middle of Fig. 2.9a is a remnant of the dead areas in PDC2 and an artifact of the algorithm. The average efficiencies for the pad chamber are about 90% at 13 mm and 85% at 11 mm, for PDC1 and PDC2 respectively.

PDC2 had to be treated somewhat differently, because of a large number of dead pads. This has led to a false splitting of clusters which created fake hits. To deal with this, only one cluster was accepted if found within 8 mm of the projected hit. For larger radii, the PDC2 chamber was treated in the same way as the other chambers.

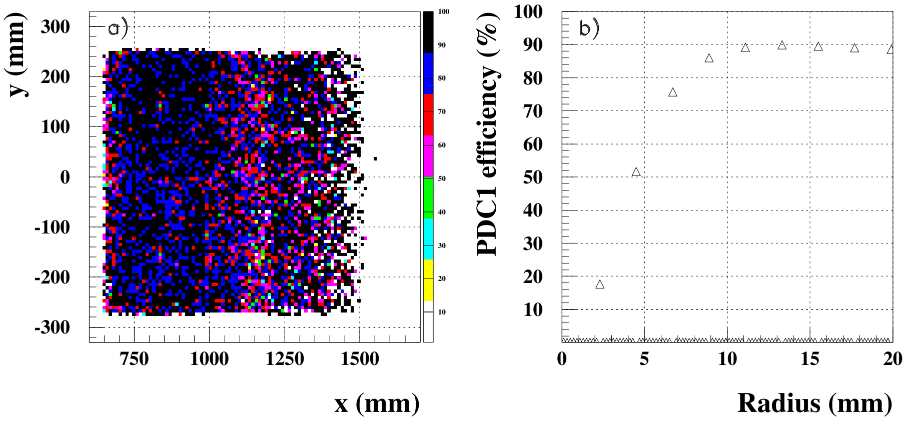

Figure 2.9: *The efficiency map for the PDC1. b) The average efficiency as a function of radius.*

The average efficiencies for the streamer tubes are approximately 91% at 18 mm and 94% at 21 mm, for STR1 and STR2 respectively. The dark vertical stripes seen in the maps are due to the overlap of two streamer tubes (see Fig. 2.3). The horizontal bands seen in both streamer tubes (Fig. 2.11a-2.12a) are present because of less sensitive areas between two readout boards.

In all efficiency maps, the rightmost parts are farthest away from

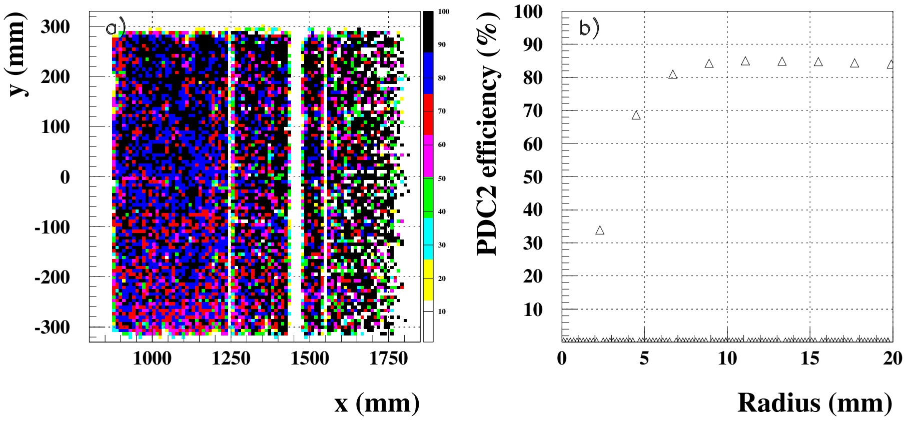

Figure 2.10: *The efficiency map for the PDC2. b) The average efficiency as a function of radius.*

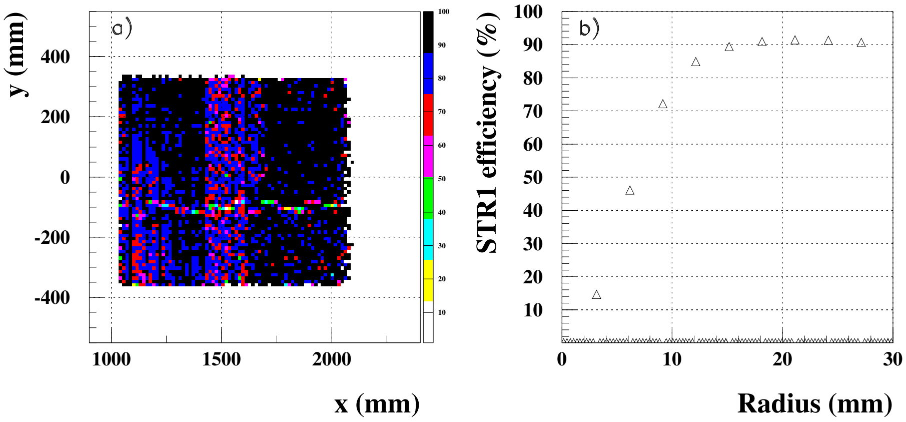

Figure 2.11: *The efficiency map for the STR1. b) The average efficiency as a function of radius.*

the beam and are subject to reduced statistics.

The background in a certain event is estimated by mixing with a different event. The clusters in this event are calculated within the same radius at the projected chamber position. It turns out, due to the relatively low occupancy, that background clusters only seem to affect the result at large radii. The average efficiency for

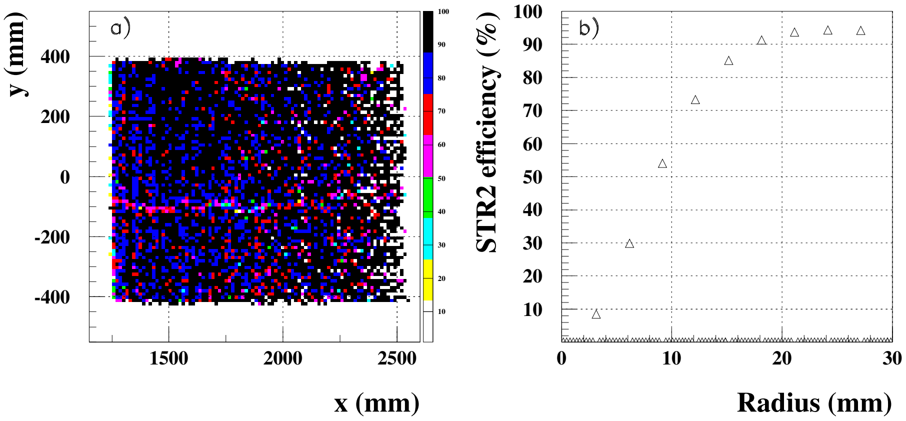

Figure 2.12: *The efficiency map for the STR2. b) The average efficiency as a function of radius.*

the pad chambers without the background subtraction is shown in Fig. 2.13, and shows that the plateau observed in the previous figures only occurs if the background is accounted for. The results are similar for the streamer tubes.

The calculated efficiency maps were used in the GEANT simulation for the analysis presented in [45].

2.4.1 Simulated efficiency maps

The efficiency algorithm was checked with a simulation, using the NEXUS event generator [10], the GEANT [11] package and the WA98 analysis code ANPACK. Events produced with NEXUS were used as input for the GEANT simulation. The output, containing information on the hits in the five chambers of the second tracking arm, was fed to the ANPACK code which smeared the hits with Gaussians but otherwise treated simulated data in the same way as raw data.

The expected performance are average efficiencies approaching 100% for all chambers, since the tracking algorithm and the chambers worked perfectly in the simulation. The actual outcome is in

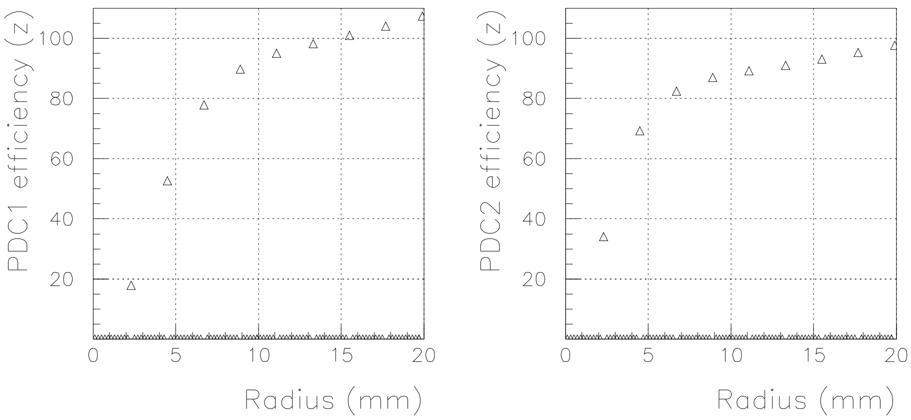

Figure 2.13: *The average efficiencies for the PDC1 and PDC2 chambers without background subtraction.*

full agreement with the expectations.

2.5 ϕ-meson production

One goal of the WA98 experiment was to study the ϕ-meson in its K^+ - K^- decay channel. The ϕ-meson has a mean life time of 1.5×10^{-22} s, while the kaons have a mean life time of about 1.2386×10^{-8} s. A kaon with a momentum of 4 GeV/c reaches the JTOF located 17.8 m from the target, after about 60 ns (see Fig. 2.14), i.e. it travels at almost 99% of c. A 1 GeV/c kaon arrives at the TOF after approximately 67 ns, implying a speed of roughly 90% of c. This means that the fastest kaons (separable from pions) travel some 30 m on the average before they decay, while the 1 GeV/c kaons only reach about 8 m. The kaons decay mostly into leptons and pions;

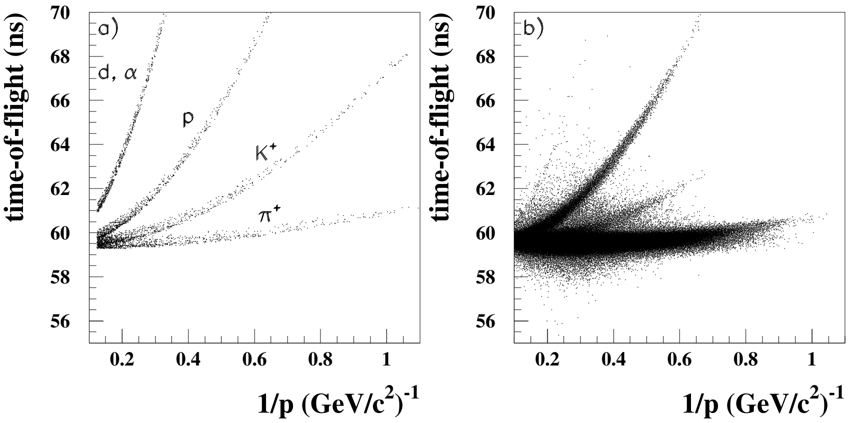

Figure 2.14: *The time of flight for pions, kaons, protons and deuterons as a function of momentum, a) calculated with the GEANT simulation package, assuming perfect detectors and no decay in flight, and b) measured from data.*

$$K^+ \rightarrow \begin{cases} \mu^+ + \nu_\mu(63.51 \pm 0.18)\% \\ \pi^+ + \pi^0(21.16 \pm 0.14)\% \\ \ldots \end{cases}$$

The K$^-$ decay modes are the charge conjugates of the above.

Due to the large mass difference between the K and the μ and π, the latter will get a large kinetic energy in the kaons rest frame, resulting in a kink on the track. As a consequence, tracks of such kaons will not be observed.

The kaons were identified by using the cuts discussed above, and the invariant ϕ-meson mass was calculated from

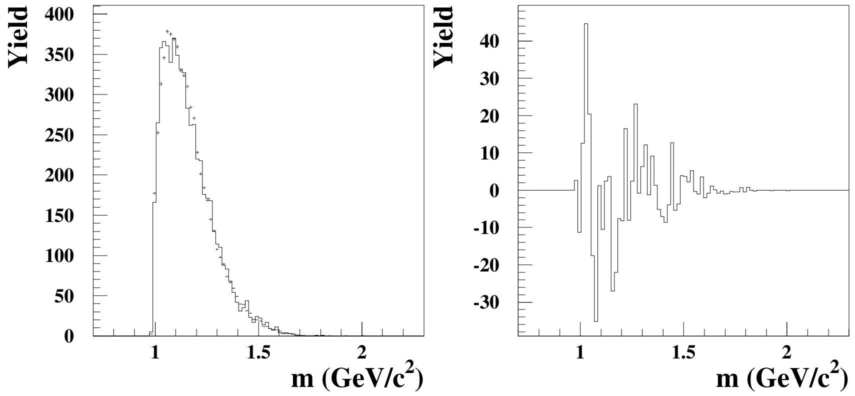

Figure 2.15: *Invariant mass distribution of the ϕ-meson. b) Background subtracted mass distribution leaving a few candidates in the 1,020 MeV/c peak.*

$$m_{inv} = \sqrt{(E_{K^+} + E_{K^-})^2 - (\mathbf{p}_{K^+} + \mathbf{p}_{K^-})^2} \tag{2.5}$$

The resulting invariant mass distribution is shown in Fig. 2.15. The background was removed with a mixed-event method, in which kaon information from several different events was combined in the mass calculation. The remaining candidates are in the narrow peak at the correct mass of 1020 MeV/c^2. Totally, 30107 K$^+$ and 25691 K$^-$ were used in this analysis.

The data set is unfortunately too small for a detailed study of ϕ-mesons, as indicated by the following discussion.

2.6 Simulation results

The event generator Fritiof [7] (version 7.02) was used to estimate the number of expected ϕ-mesons within our acceptance. In 10500 events, kaons coming from ϕ-mesons were simultaneously detected 121 times. As the data analysis is based on 122373 events, we should get about 1 400 ϕ-mesons within the acceptance. However, this should be corrected for the tracking efficiencies in the arms (roughly 50% each). A large fraction of the kaons is also lost due to decay. Out of all 4 GeV/c kaons about 55% have survived at the JTOF and roughly the same fraction at the RTOF. The 1 GeV/c kaons only have a 10% chance, in each arm, of lasting that long. Averaging over the momentum gives an average loss of 83% in the observed number of ϕ-mesons, i.e. only 1/6 of the ϕ decays, within our acceptance, survive for detection.

2.7 Discussion and conclusion

A ϕ-meson analysis has been presented. The found ϕ-candidates lie in a narrow peak at the correct mass of 1 020 MeV/c^2. The analysis indicates that it was possible to resolve the ϕ-resonance in the WA98 experiment in the $K^+ - K^-$ channel using the two tracking arms with data from the 1996 $Pb + Pb$-run. Unfortunately, the experiment ended its data taking before we could gather enough statistics for a more systematic study of the ϕ-meson and its properties.

Due to the limited statistics it is impossible to quantify the studies of the ϕ-meson production. We can only conclude that the observations do not disagree with the Fritiof simulation.

Chapter 3

The PHENIX Experiment

The PHENIX experiment [46, 47] is one of the four[1] large experiments at the Relativistic Heavy Ion Collider (RHIC) at Brookhaven National Laboratory in the United States. The collider was ready to deliver ^{197}Au beams with an energy of 65 A GeV per beam in the summer of 2000. For the second run in 2001, the energy was increased to 100 A GeV per beam. This chapter presents the experiment, a technical overview and performance of the Pad Chamber reconstruction software as well as a single particle spectral analysis based on 65+65 A GeV data.

3.1 Physics objectives

The primary goals of the experiment are to detect and study the properties of the quark-gluon plasma and to characterize its nature. Of the many suggested experimental probes of the plasma, the PHENIX detector will simultaneously measure most of the potential signatures.

The strategy is to study photon, lepton and hadron signals un-

---

[1] The other being the STAR, PHOBOS and BRAHMS experiments.

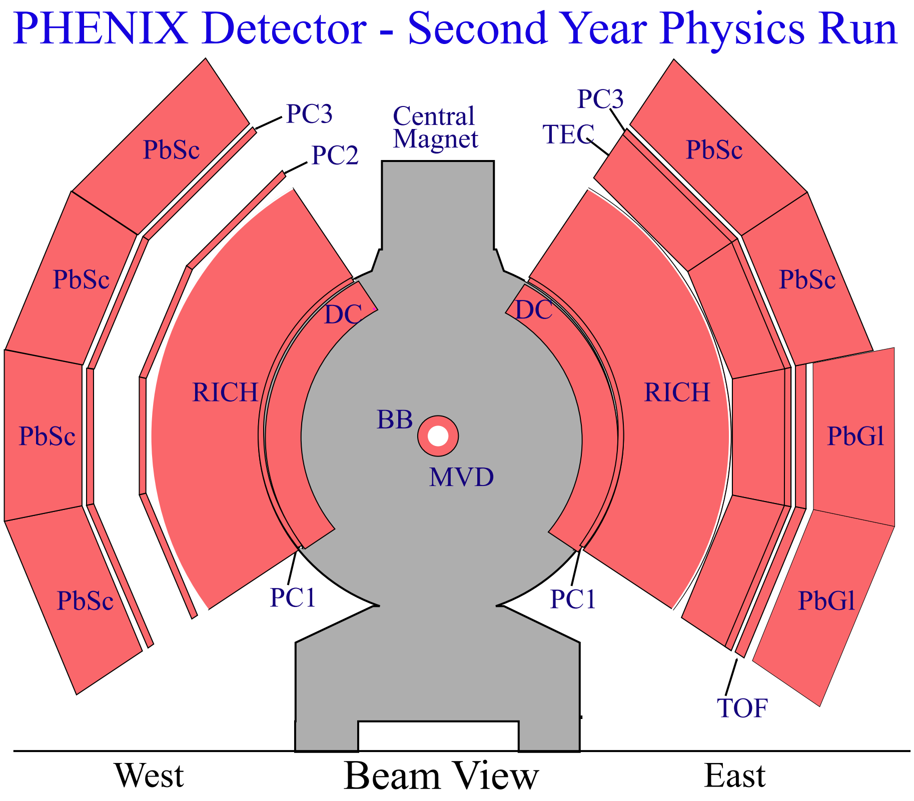

Figure 3.1: *A cut-view of the PHENIX detector system.*

der the same experimental conditions. The photons and leptons are created in the plasma and can therefore be used to give direct information of the QGP phase. The more copiously produced hadrons, will provide complementary information about the hadronization phase transition.

PHENIX also has an extensive spin physics program [48], since RHIC has the capability to collide beams of polarized protons.

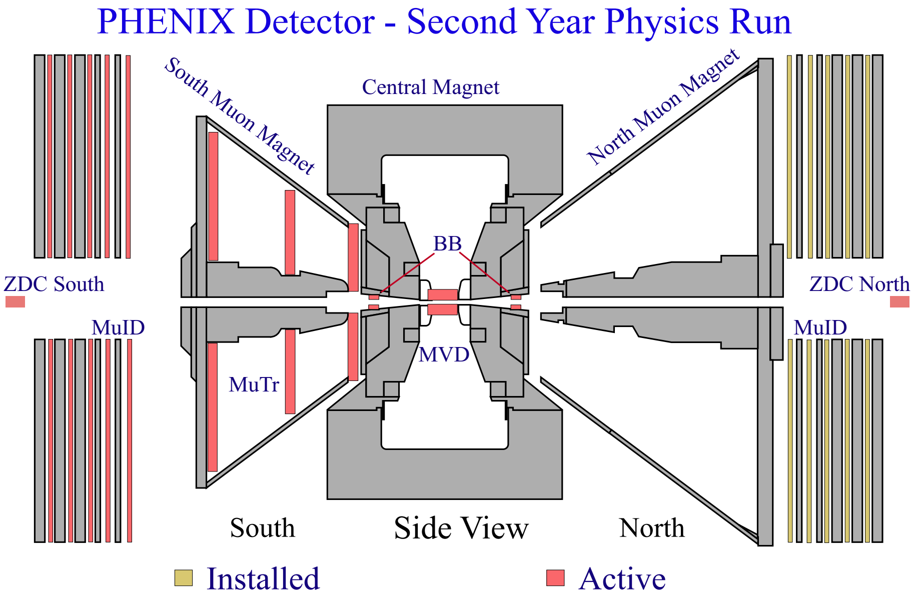

Figure 3.2: *A cut-view of the PHENIX detector system.*

3.2 The PHENIX subsystems

The PHENIX detector consists of several subsystems, divided into two central arms, two muons spectrometers and the inner detectors (Fig. 3.1 and Fig. 3.2). The central arms detect charged particles and photons, while the muon spectrometers measure muons. The vertex position, start time and multiplicity are measured by the inner detectors.

The magnets. This subsystem is comprised of a central magnet (CM) and two muon magnets (MM). The central magnet, with a height of 9.5 m and a weight of nearly 500 tons, surrounds the collision point and produces an axial field parallel to the beam. The maximum bending power is designed to be 1.0 Tm when integrated to a radius of 4.0 m. At a radius of 2.0 m, where the first tracking chamber is located, the field strength is weak.

The muon magnets produce radial magnetic fields with the help of two solenoidal coils each. When integrated from 2.0-6.0 m in the z-direction along a line 15° from the beam axis, the radial field component is 0.72 Tm. The MM:s weigh more than 400 tons each with heights of 10.5 m.

The inner detectors. Located close to the collision zone, a set of inner detectors provide a centrality trigger, event characterization, the collision vertex position and the time-of-flight start time. Fluctuations in the charged particle distributions can also be measured by these detectors.

The Multiplicity Vertex Detector (MVD), installed for the second run (run-2), will measure the vertex position of the interaction, the charged particle multiplicity and provide a centrality trigger [49]. It will also provide the pseudorapidity distribution of charged particles. The vertex can be found with good precision for z-positions up to $\pm$ 40 cm. Silicon pad detectors, placed at the MVD end caps, will measure the $dN_{ch}/d\eta$ distribution of large rapidity particles.

The start time for the time-of-flight is provided by the two Beam-Beam Counters (BBC), consisting of 64 photomultiplier tubes equipped with quartz Čerenkov radiators [50]. The counters are clustered around the beam pipe at 1.44 m upstream and downstream of the beam crossing point, intercepting particles at large rapidities ($3.0 < \eta < 3.9$). The BBC's are also used to generate the primary interaction trigger, by requiring at least two fired photomultipliers in each counter and a collision vertex position of $|z| < 30$ cm.

The Zero Degree Calorimeters are small hadron calorimeters that measure neutron energy within a 2 mrad cone around the beam pipe. The ZDC's are placed at large distances from the inner detectors, at $\pm$ 18 m from the center of the interaction region. In combination with the BBC's, the ZDC's are used for event selection in the offline analysis (see Fig. 3.9).

The muon spectrometers. Designed to give PHENIX acceptance for particles decaying into lepton pairs emitted at large rapidities, the muon arm detector elements perform charged particle tracking, momentum analysis and muon identification. Multilayer cathode strip chambers (μT) measure the particle trajectories, while the muon identifier (μID) distinguishes muons from pions and other showering products. The mass resolution is sufficient to also resolve ψ' from J/ψ and the Υ (2S+3S) from Υ (1S). Since most hadrons are stopped by the central magnet poles, the multiplicities in the muon arms are fairly low.

The central arm spectrometers. The two central arms, called east and west, each cover 90° in azimuth (ϕ), and are separated by 67.5° in the upper part and 112.5° in the lower. The subsystems perform charged particle tracking and momentum measurements, photon and electron energy measurements as well as identification of various particle species and resonances (ρ, ω, ϕ, etc).

Located at radial distances of 2 m from the collision zone, the Drift Chambers (DC) trace charged particles (primarily in r/ϕ) and provides a high resolution p_T measurement [51].

The Pad Chamber layers, called PC1-3, are located at radial distances of 2.5, 4 and 4.9 m [paper II and IV in this thesis]. The Pad Chambers are tracking chambers that perform space point measurements used in pattern recognition and momentum determination for charged particles. PC2 is installed in the west arm only.

The Ring-Imaging Čerenkov counter (RICH) is placed after PC1 between the inner and outer group of tracking chambers [52, 53]. Being the primary device for electron identification in PHENIX, it provides e/π discrimination below the pion Čerenkov threshold, set to about 4 GeV/c.

The Time Expansion Chamber (TEC) is positioned at approximately 4.1 m from the collision region in the east central arm. It measures track position and energy deposition along the track [54]. By measuring dE/dx, the TEC is able to separate electrons from pions up to about 1 GeV/c.

The Time-Of-Flight wall (TOF) is placed outside PC3E and covers one third of a central arm [same TOF as in the WA98 experiment, see paper I]. It measures the time-of-flight of charged hadrons over a large momentum range. Pions and kaons can be separated up to a momentum of 2.4 GeV/c[2]. The intrinsic position resolution is 85 ps.

The primary role of the Electromagnetic Calorimeter (EMCal) is to identify photons and electrons, to measure their energies and positions, and as a trigger for rare events where photons and electrons are produced with high p_T [55]. Electrons can be identified below 350 MeV/c by time-of-flight and above 1 GeV/c by energy-momentum matching. Kaons and electrons can be separated by time-of-flight up to 1 GeV/c. *Pb* glass from the WA98 experiment constitutes 25% of EMCal. The EMCal is the detector system located farthest away from the collision zone, at about 5.1 m.

The PC1/DC form the inner tracking unit and the PC2/TEC/PC3 form the outer tracking unit which link the track segments traversing the RICH and extending to the TOF and the EMCal.

The Pad Chambers. In the original design there were three thin layers of pad chambers in each central arm (Fig. 3.3). Due to financial reasons, this was changed to having only one layer of the PC2 chambers. The final design has a total area in both arms of about 88 m^2. PC1 has eight flat sectors of Multi-Wire Proportional Chambers (MWPC:s) per arm, while PC3 has four sectors. PC2 also has four installed sectors, but only in one arm. The chambers are read out by induced signals on the cathode planes, that are finely segmented in pads [56].

From the signals on the pads, cells are formed from which the actual hits are reconstructed (see section 3.3). The size of a cell is approximately of the desired position resolution, which is a few mm in z and r/ϕ (see section 3.4.4 below).

The entire readout system consists of 172 800 readout channels, where the readout is on a Yes/No basis. The occupancy at a typical central $Au + Au$ event is 2%, thus providing very clean hit infor-

---

[2] The number is given for a fully calibrated TOF. During the first run (run-1) pions and kaons could be separated up to 1.7 GeV/c.

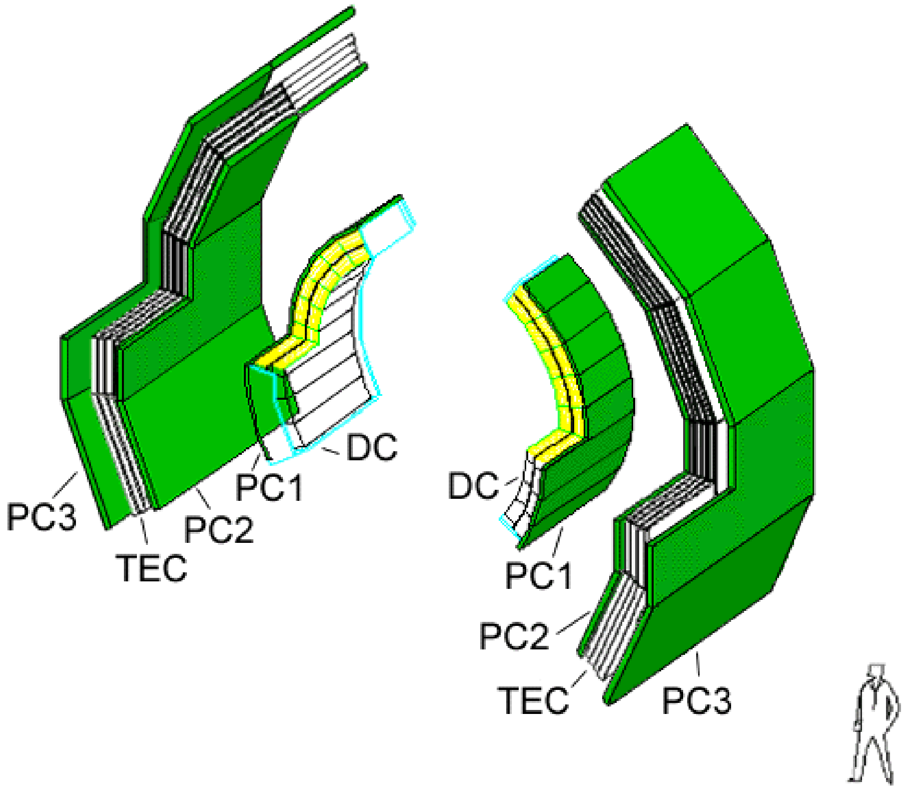

Figure 3.3: *A cut-view of the PHENIX pad chambers with identical tracking arms. The original design was changed due to financial reasons to having only one PC2 (west arm) and one TEC (east arm).*

mation. For the other PHENIX tracking detectors, the occupancies are up to 10%. The readout system is further discussed in papers II and IV.

3.3 The pixel readout of the Pad Chambers

The illustration in Fig. 3.4 shows a part of the pixel system. A pixel is a small copper electrode that is connected to eight other pixels. All nine pixels are read out by one single amplifier/discriminator.

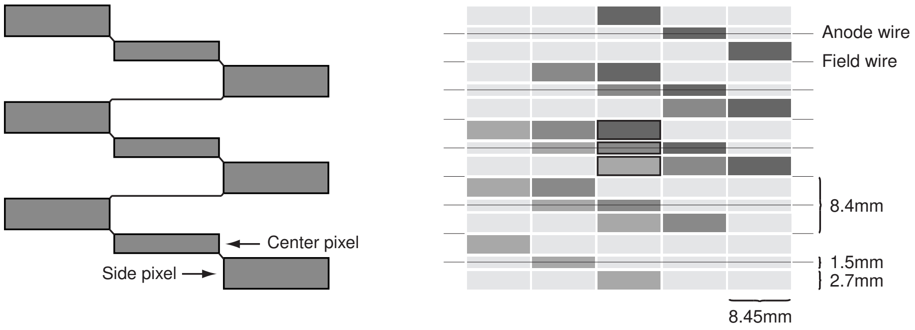

Figure 3.4: *Pad consisting of nine pixels (left). The pad chamber pixel layout showing three fired pads and a cell (right). The dimensions are for PC1.*

The group of nine pixels is called a pad. The pads are interleaved with each other in a repeated pattern. Finally, a cell is a group of three pixels belonging to three different but adjacent pads. This arrangement saves a factor of three in the number of readout channels with marginal loss of performance compared to a straight forward readout concept of quadratic pads of the size of a cell.

The size of the pixels has been chosen to collect an equal amount of charge. The side pixels are somewhat larger than the center pixels that are closer to the avalanche. Thus the side and center pixels collect approximately equal fractions of the avalanche charge. As we demand that three neighbouring channels have to fire to form a valid hit, the system will consequently be totally immune against electronics noise which normally is a complication in discriminator based readout systems.

3.4 Reconstruction

The response of the pad chambers is being simulated within the PHENIX software framework. The event generator HIJING1.35 [9] has been used to feed the PHENIX GEANT [11] simulation package, called PISA, with events. PISA tracks the particles through the detector system. The hit information is stored in large event files, which are then used as input for the reconstruction code.

3.4.1 The response simulator

The PISA hit information is processed with a response simulator. For each track, the deposition of charge on the chamber wires is estimated using a Landau distribution with the addition of random electronics noise. The output is a list of all pads that have received charge above a certain threshold.

3.4.2 The cluster reconstruction algorithm

The cluster reconstruction code reads the list of fired pads and translates it into a list of cells, which is more easy to work with. The outline of the main algorithm (Fig. 3.5) is to first identify a group of one or more cells, called a cluster, and then process each cluster separately to determine the original hit position. The used cells are removed from the list. The number of particles that have created the cluster is estimated by analyzing the cluster size. If the number is larger than one, the cluster is split into subclusters according to size and symmetry arguments. The last step of the algorithm calculates the center of each subcluster and transforms it from cell space into the global PHENIX coordinate system.

The stored hit information is used in the track finding and the momentum reconstruction. When possible, the DC uses the PC1 z-coordinates to define the tracks.

3.4.3 Cluster splitting

When two or more charged particles pass through a chamber at close distance from each other, charge is deposited on many pads

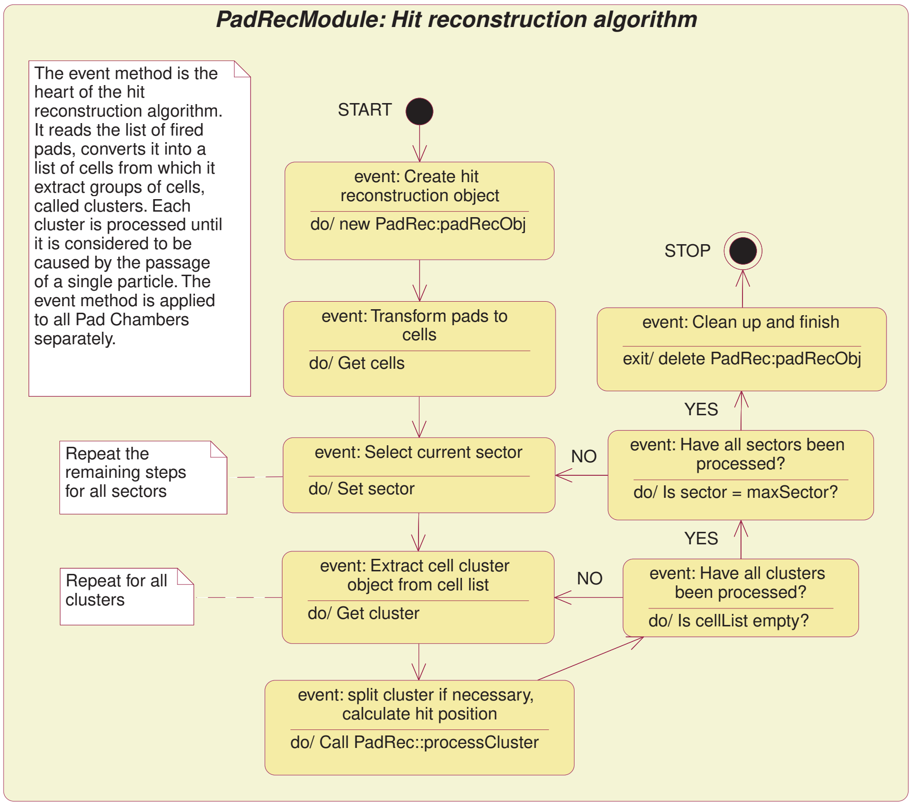

Figure 3.5: *UML state transition diagram showing the program flow of the PC cluster reconstruction algorithm.*

resulting in a large cluster of several cells. In order not to loose resolution in the Pad Chambers, these large clusters need to be split until each sub cluster is considered to be caused by a single charged particle. Fig. 3.6 describes in detail how the split algorithm works. Using the cluster split algorithm recovers about 34 % of the hits that otherwise will be lost due to cluster overlap.

The resolution plots in the following sections for simulated data were all generated with cluster splitting turned on. With real data the picture is more complicated due to large clusters created by single particles entering sideways in the chamber, long range delta

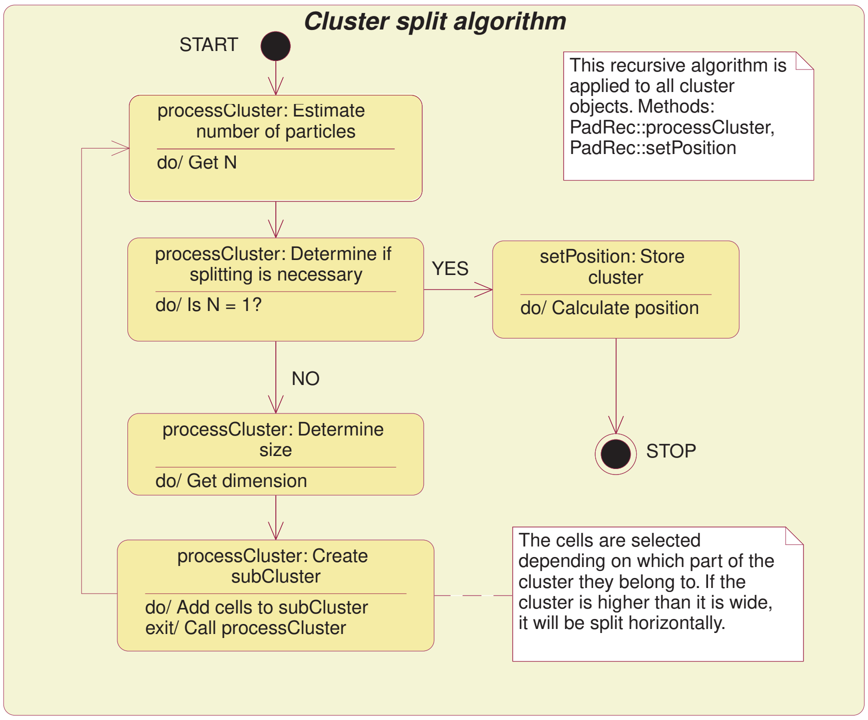

Figure 3.6: *If a cluster is considered to be caused by the close passage of two or more tracks, it will be split until each subclusters is a single-particle cluster. The UML state transition diagram shows the program flow of the recursive split algorithm.*

electrons, slow moving highly ionizing protons, sparks, etc. These effects are subject to continued studies. The multiplicity study described in paper V was done without cluster splitting.

3.4.4 Position resolutions

The simulated PC1 position resolution is shown in Fig. 3.7. The reconstructed hit positions were compared to the true hit positions

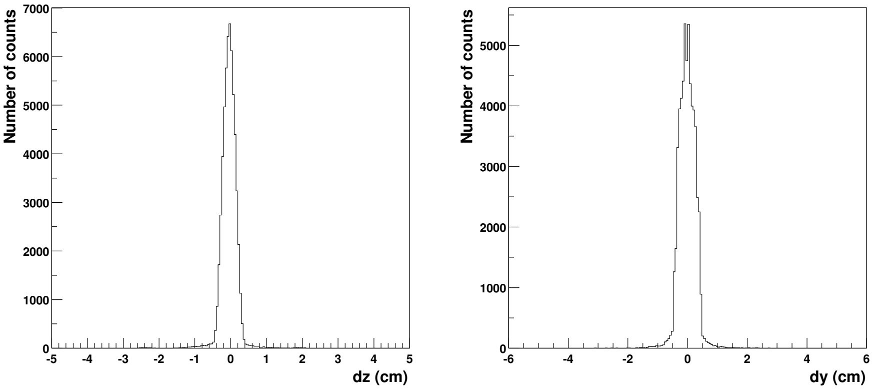

Figure 3.7: *The simulated position resolution in PC1 along (z) and across (y) the wire.*

according to

$$\begin{cases} \Delta y = y_{REC} - y_{PISA} \\ \\ \Delta z = z_{REC} - z_{PISA} \end{cases} \tag{3.1}$$

where y is the coordinate across the wires and z is the coordinate along the wires, which is also along the beam direction.

The position resolutions were also experimentally estimated using cosmics. The details of this study can be found in Paper IV. Table 3.1 shows the position resolutions from both simulation and measurements.

3.4.5 Two-track resolutions

By simulating minimum ionizing π^+ pairs with small separation in PISA, the probability for resolving nearby tracks was calculated. The momenta of the pions were chosen as the rule of thumb value of 500 MeV. A more careful calculation gives that the momentum of a minimum ionizing pion is about 460 MeV with $\beta = 0.957$. The

Table 3.1: Measured and simulated position resolutions (rms values).

Measured	PC1 σ (mm)	PC2 σ (mm)	PC3 σ (mm)
Along wire	1.7	3.1	-
Across wire	3.4	5.0	-
Simulated	PC1 σ (mm)	PC2 σ (mm)	PC3 σ
Along wire (split)	1.6	2.7	3.2
Across wire (split)	2.3	4.0	4.8
Along wire (no split)	2.4	4.0	4.9
Across wire (no split)	2.8	5.5	6.1

two-track resolution is in this context defined as the distance where 50% of the tracks are separated. Shown in Fig. 3.8 are the two-track resolutions along and across the wires for PC1. Numbers are given in Table 3.2.

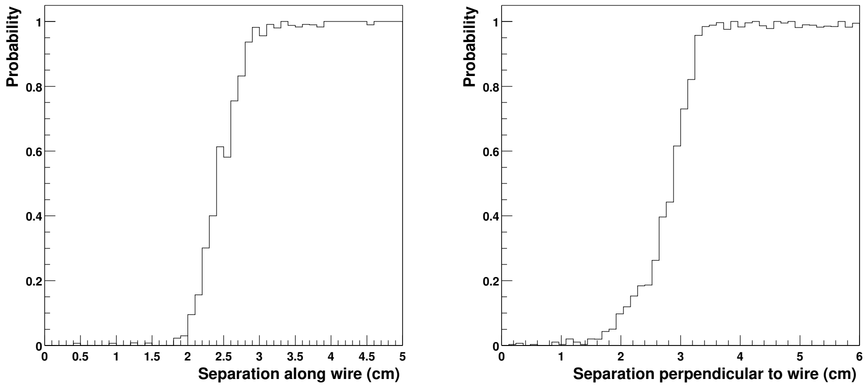

Figure 3.8: *The two-track resolution along the wires for PC1. b) The two-track resolution across the wires for PC1 estimated with simulated data.*

Table 3.2: Two-track resolutions of the Pad Chambers along and across the wire as estimated with simulated data.

With cluster splitting	PC1	PC2	PC3
Along wire (cm)	2.4	4.0	5.0
Across wire (cm)	2.9	4.6	5.3
Without cluster splitting	PC1	PC2	PC3
Along wire (cm)	3.5	5.8	6.6
Across wire (cm)	3.0	5.0	5.7

3.5 Single particle spectra

Inclusive single particle spectra for identified pions, kaons and protons have been studied for different centralities at $\sqrt{s} = 130$ A GeV. This section summarizes the analysis methods and the first results[3].

3.5.1 Event and track selection

By correlating the total charge in the BBC's with the total energy deposited in the ZDC's, we can define distinctive centrality classes. The ZDC's are sensitive to spectator neutrons while the BBC's measure produced particles from the participant volume. In a central event there will be less neutrons in the ZDC's, while the number of measured particles in the BBC's will be large. In a peripheral event there will be a small number of measured particles in both the ZDC's and the BBC's. A not-so-central event will produce the largest signal in the ZDC's, while the BBC signals will be intermediate.

The analysis is based on 75k minimum bias events (highest quality selection) that has survived the cuts given below, divided

---

[3] The presented analysis is one of several agreeing parallel studies in PHENIX. The corresponding official PHENIX preliminary data is available in the Quark Matter 2001 proceedings.

Table 3.3: Definition of centrality classes.

Centrality class	Percentile
Most central	0-5%
Central	5-15%
Not so central	15-30%
Semi peripheral	30-60%
Peripheral	60-92%

into the five centrality classes defined in Table 3.3 and shown in Fig. 3.9. The most central event selection corresponds to 5% of the inelastic cross section, etc. The inelastic cross section was calculated with RQMD2.4 [8] to $\sigma^{RQMD}_{inelastic} = 7.1 \pm 0.3$ barn.

The hardware trigger for this analysis was chosen as a signal from either the ZDC, the BBC or in both the ZDC and the BBC (Fig. 3.9). To avoid tracks passing too close to the magnet poles, a vertex cut of ± 30 cm was applied. A momentum dependent hit association cut of 2σ in z and ϕ of the projected DC/PC1 track to the TOF was applied in order to increase the track quality further. It was also checked that each track had a dE/dx in the TOF slat that was consistent with the measured velocity. If the deposited energy was too low, the track was rejected. In order to better match the acceptance between data and simulation, fiducial cuts in the DC were applied due to dead areas in the chamber.

3.5.2 Particle identification

The high resolution TOF was used to identify pions, kaons and protons. Fig. 3.10 shows the mass squared-momentum space for all accepted tracks. The dashed curves show the location of the $2\sigma_{m^2}$ limits used in the analysis.

Assuming that the error in the track length L is negligible, the errors in m^2 can be calculated from

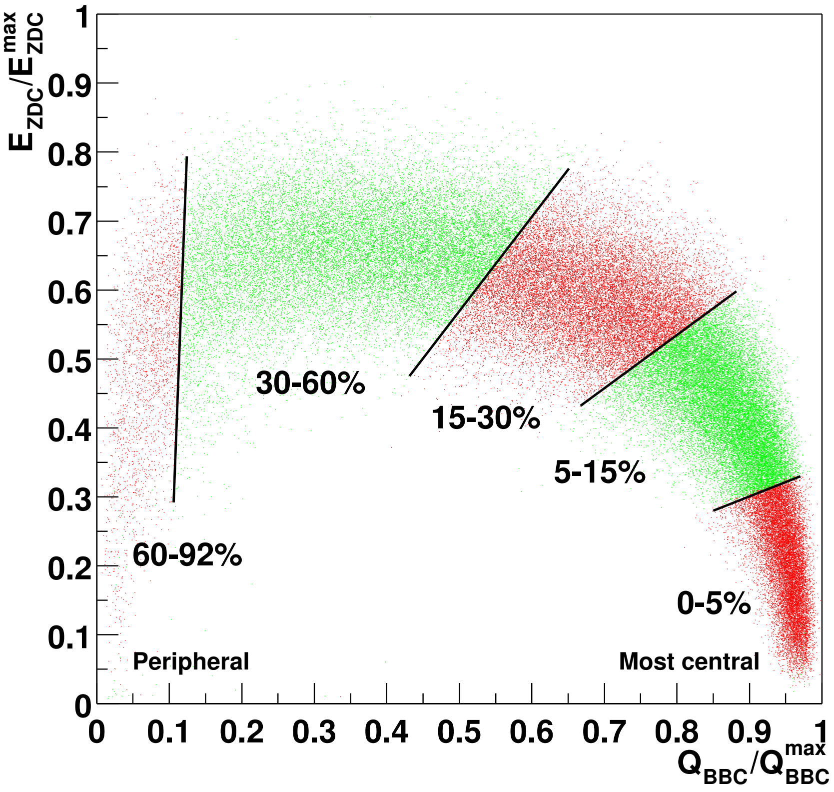

Figure 3.9: *Centrality selection with the ZDC and BBC calorimeters.*

$$\sigma_{m^2}^2 = \frac{\sigma_\alpha^2}{K^2}(4m^4p^2) + \frac{\sigma_{ms}^2}{K^2}(4m^4(1+\frac{m^2}{p^2})) + \frac{\sigma_t^2 c^2}{L^2}(4p^2(m^2+p^2)) \quad (3.2)$$

where the first two terms correspond to the error in momentum, due to position resolution and multiple scattering, and the last to the error in timing. Calculated from data, the timing error was found to be $\sigma_t = 125 \pm 5$ ps, while the simulated multiple scattering

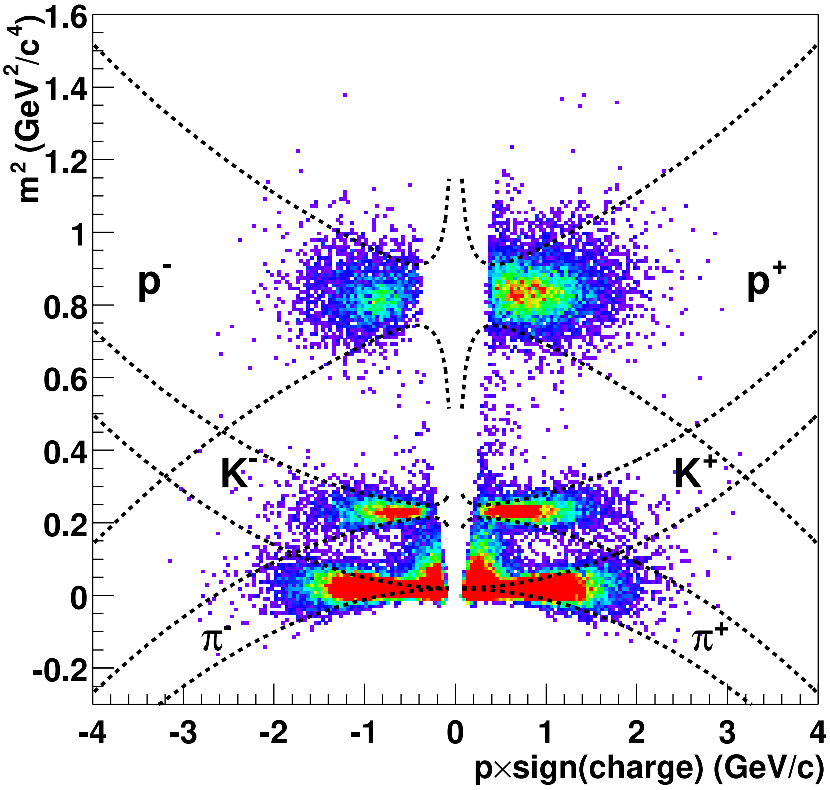

Figure 3.10: *Particle bands showing identified pions, kaons and protons. The dashed lines correspond to the* $2\sigma_{m^2}$ *limits (PID limit) used in the identification.*

resolution was estimated to $\sigma_{ms} = 0.3 \pm 0.1$ mrad. The magnetic field energy, given by

$$K = \frac{c}{R_{DC}} \int Bldl \tag{3.3}$$

is approximately 84 mrad GeV, with a reference DC distance of

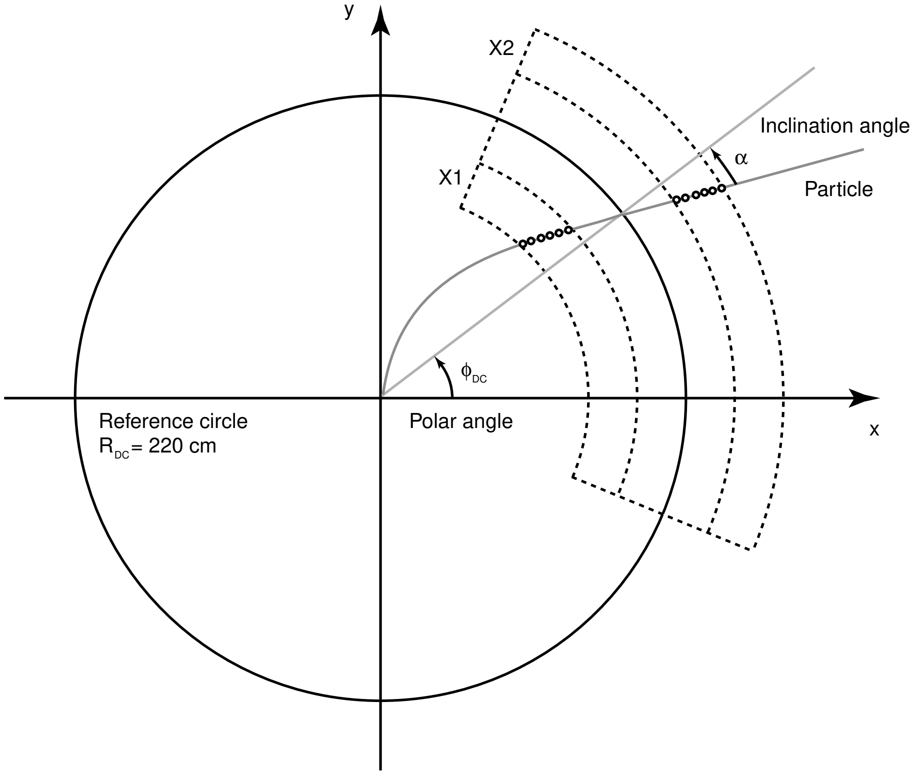

Figure 3.11: *Track passing through the DC, defining the inclination angle α, the reference distance R_{DC} and shows the location of the X1 and X2 wire planes.*

$R_{DC} = 2.2$ m. The track resolution σ_α was estimated from simulation to 3.0 ± 0.5 mrad for partially reconstructed DC tracks using the X1 or X2 wires planes. The inclination angle and the reference distance are defined in Fig. 3.11.

The consistency with data was checked for all relevant momentum intervals by comparing the standard deviations calculated from Eq. 3.2, shown in Table 3.4, with the standard deviations from Gaussian fits of measured m^2. The latter are listed in Table 3.5.

Table 3.4: Calculated standard deviations. The PID limits use 2σ cuts.

p (GeV/c)	$\sigma^{\pi^\pm}_{m^2}$ (GeV^2/c^4)	$\sigma^{K^\pm}_{m^2}$ (GeV^2/c^4)	$\sigma^{p^\pm}_{m^2}$ (GeV^2/c^4)
0.4	0.003	0.010	0.041
0.6	0.006	0.013	0.046
0.8	0.010	0.018	0.056
1.0	0.015	0.025	0.068
1.2	0.022	0.032	0.082
1.4	0.030	0.040	0.096
1.6	0.039	0.049	0.111
1.8	0.049	0.060	0.127
2.0	0.060	0.071	0.143
2.2	0.073	0.084	0.160
2.4	0.087	0.099	0.178
2.6	0.102	0.113	0.196
2.8	0.118	0.129	0.216
3.0	0.135	0.146	0.236
3.2	0.154	0.165	0.257
3.4	0.174	0.185	0.28
3.6	0.195	0.206	0.303

3.5.3 Background analysis

At lower momenta, pions, kaons and protons are well separated. As momentum increases, the pion and kaon bands move closer and become difficult to separate above 1.7 GeV/c since the pion background in the kaon peak becomes large. Protons are well separated from kaons at all momenta considered in this analysis.

Table 3.6 lists the background percentages in the kaon spectra as estimated from data. The background is mostly pions, but also has an exponential contribution of tracks with wrongly correlated momenta and time-of-flight. Within $2\sigma_{m^2}$ of the pion peak, the kaon contribution is negligible for all momenta. This is also the case of the protons which do not contribute to the kaon or pion spectra.

Table 3.5: Standard deviations from Gaussian fits to m^2 of positive and negative particles (data). The numbers are calculated within $p \pm$ 0.1 GeV/c.

p (GeV/c)	$\sigma_{m^2}^{\pi^+}$ (GeV^2/c^4)	$\sigma_{m^2}^{K^+}$ (GeV^2/c^4)	$\sigma_{m^2}^{p^+}$ (GeV^2/c^4)
0.6	0.006	0.014	0.060
0.8	0.011	0.018	0.055
1.0	0.017	0.023	0.061
1.2	0.023	0.029	0.062
1.4	0.032	0.036	0.075
1.6	0.039	0.041	0.075
p (GeV/c)	$\sigma_{m^2}^{\pi^-}$ (GeV^2/c^4)	$\sigma_{m^2}^{K^-}$ (GeV^2/c^4)	$\sigma_{m^2}^{p^-}$ (GeV^2/c^4)
0.6	0.006	0.016	0.057
0.8	0.011	0.021	0.050
1.0	0.017	0.026	0.067
1.2	0.023	0.032	0.077
1.4	0.031	0.034	0.091
1.6	0.038	0.035	0.086

A comparison is also made with and without requiring a hit associate in PC3 (located in front of the TOF) for the track. The background is somewhat suppressed since the track is better defined if PC3 is included. Unfortunately this also suppresses the statistics which is reduced by 25 %.

3.5.4 Corrections

Correction factors for pions, kaons and protons were estimated from a single particle Monte Carlo to correct for geometrical acceptance, decay in flight, tracking efficiency and residual matching cuts to the TOF. Fig. 3.12 shows the correction factors for all relevant particles. Anti-particles, shown as dashed lines, have a slightly different acceptance than normal particles, due to the non-symmetric posi-

Table 3.6: Background levels (%) in kaon spectra within $2\sigma_{m^2}$ as estimated with 75 000 minimum bias events. The momentum is given in GeV/c.

p±0.1	$N^{NoPC3}_{bg,\pi^+}/N_{K^+}$	$N^{PC3}_{bg,\pi^+}/N_{K^+}$	$N^{NoPC3}_{bg,\pi^-}/N_{K^-}$	$N^{PC3}_{bg,\pi^-}/N_{K^-}$
0.6	3.7±0.5	2.3±0.5	5.0±0.8	3.9±0.4
0.8	3.1±0.5	2.3±0.5	4.1±0.7	3.7±0.3
1.0	4.3±0.7	3.8±0.8	6.0±1.0	4.7±0.5
1.2	7.4±1.0	5.4±1.0	9.4±1.5	8.1±1
1.4	17.0±2.0	12.6±2.0	19.7±2.7	22.1±8
1.6	18.6±2.6	9.2±2.2	45.9±4.0	3.8±1.8

tion of the TOF relative to the DC.

In order to avoid the systematic effects introduced by using fit correction functions which tend to smooth the simulated acceptance, the spectra shown in the following sections should instead be corrected bin-by-bin. This is however a long term project since it requires much more statistics than in the present analysis which will take a long time to push through PISA.

In addition to these correction factors, the background as estimated in section 3.5.3 above, was also used to correct the kaon spectra in the following sections[4].

3.5.5 Transverse momentum spectra

The corrected p_T spectra for the five centrality classes are shown in Fig. 3.13 for pions, kaons and protons respectively. A minimum bias comparison with simulated data is shown in Fig. 3.14.

---

[4] The background corrections for pions and protons were negligible.

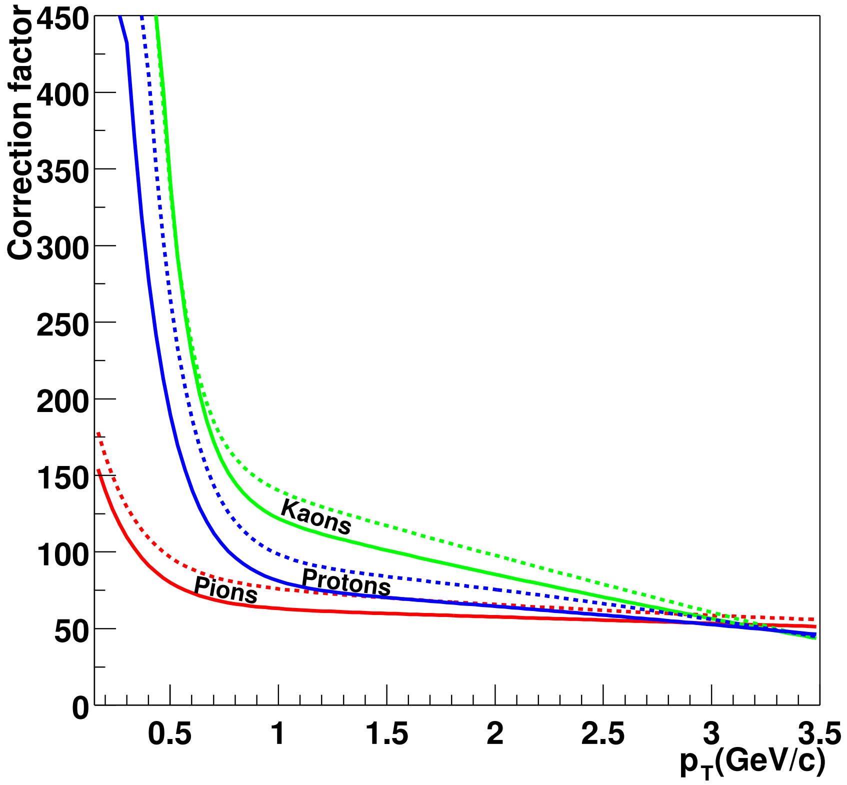

Figure 3.12: *Correction curves for pions, kaons and protons. Dashed lines correspond to anti-particles.*

3.5.6 The inverse slope parameters

In order to extract the inverse slopes, T_{eff}, an exponential function of the form

$$\frac{1}{m_T}\frac{dN}{dm_T} = Ae^{-\frac{m_T}{T_{eff}}} \tag{3.4}$$

was fit to the transverse mass spectra for positive and negative particles. The results for the five centrality classes are given in Table 3.7 (the errors are statistical only). The pions were fit for $0.3 < p_T < 0.9$ and the kaons and protons between $0.55 < p_T < 1.6$.

The extracted inverse slopes for minimum bias data are shown in Table 3.8 together with simulated data.

Table 3.7: Inverse slope parameters of all identified particles for the five centrality classes.

Centrality	π^+	K^+	p
Most central	180±2	234±8	304±13
Central	175±1	235±6	292±10
Not so central	170±1	234±6	282±9
Semi peripheral	164±1	223±6	251±9
Peripheral	155±3	190±15	202±16
Centrality	π^-	K^-	$\overline{p}$
Most central	177±3	256±10	352±18
Central	174±2	247±7	361±15
Not so central	176±2	261±9	325±13
Semi peripheral	168±2	246±9	294±11
Peripheral	152±4	205±15	235±25

Shown in Fig. 3.15 are the inverse slope parameters from Table 3.7 for all identified particles as a function of the rest mass of the particles. As can be seen in the figures, the slopes increase with centrality which is consistent with earlier observations at the SPS [57, 58] and the AGS [59], and was attributed to collective transverse flow. At more peripheral events, the slopes tend to level out, as is expected.

Table 3.8: Inverse slopes of all identified particles for minimum bias data together with simulated data.

Particle	$T_{eff}^{DATA}(MeV)$	$T_{eff}^{RQMD}(MeV)$	$T_{eff}^{HIJING}(MeV)$
π^+	180±2	137±1	126±1
π^-	177±3	134±1	130±1
K^+	233±8	170±12	171±16
K^-	287±16	197±28	163±29
p	304±13	169±28	355±197
$\overline{p}$	348±19	211±141	317±298

3.6 Discussion and conclusion

An analysis based on PHENIX run-1 (65+65 A GeV) data has been presented. Preliminary transverse momentum spectra has been shown for five centrality classes (Fig. 3.13) and has been compared to the RQMD2.4 [8] and HIJING1.35 [9] models for minimum bias events (Fig. 3.14). Inverse slope parameters from transverse mass spectra was extracted (Table 3.7) and compared to simulations (Table 3.8). Plotting the inverse m_T slopes versus the rest masses for all identified particles (pions, kaons and protons) gives at hand that the T_{eff}-parameter increases with centrality (Fig. 3.15). At more peripheral collisions, it levels out as is expected since the system more resembles a *pp*-collision.

In a purely thermal picture, T_{eff} would represent the temperature of the system at the time of freeze-out. However, the mass dependence of T_{eff} is observed to be linear and can be parametrized as

$$T_{eff} = T_{freeze-out} + km \tag{3.5}$$

where the parameters are interpreted as the freeze-out temperature (the intercept) and a constant proportional to the square of the collective flow velocity (the slope) respectively. The intercepts varies between (158±3) MeV to (146±5) MeV (most central to peripheral) for positive particles and (146±4) MeV to (136±6) MeV for negative particles. We consider, however, the statistical significance in our data not to be sufficient to clearly establish the linear dependence. Even if this was established, the interpretation of the parameters may not be the only possible.

The parameterizations, both of the inverse slopes and their mass dependencies are however viable tools for systematizing the obtained spectra and to condense the information in a few numbers by which different data become comparable.

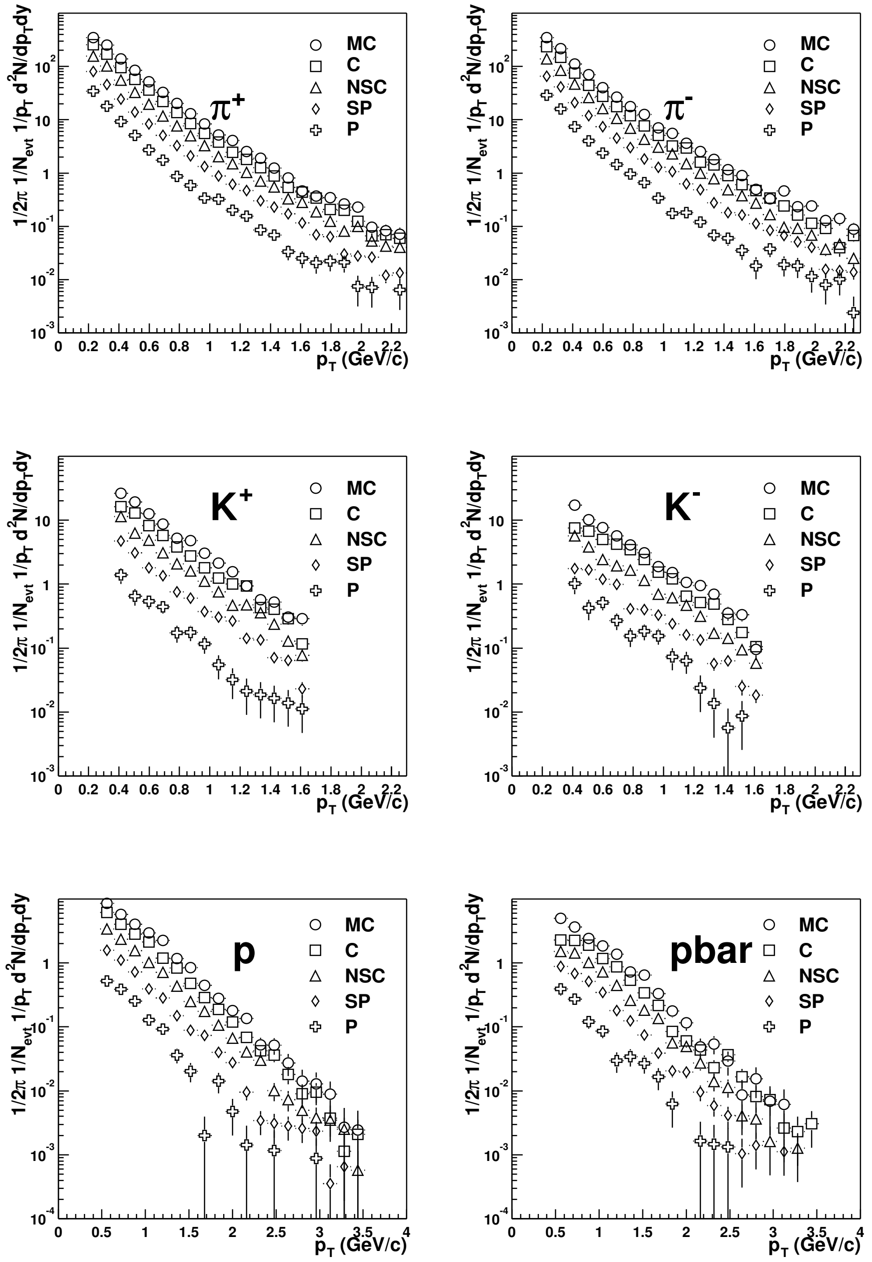

Figure 3.13: *p_T spectra for identified pions, kaons and protons in the five event classes; most central (scaled to ×1), central (×0.8), not so central (×0.6), semi peripheral (×0.4) and peripheral (×0.2).*

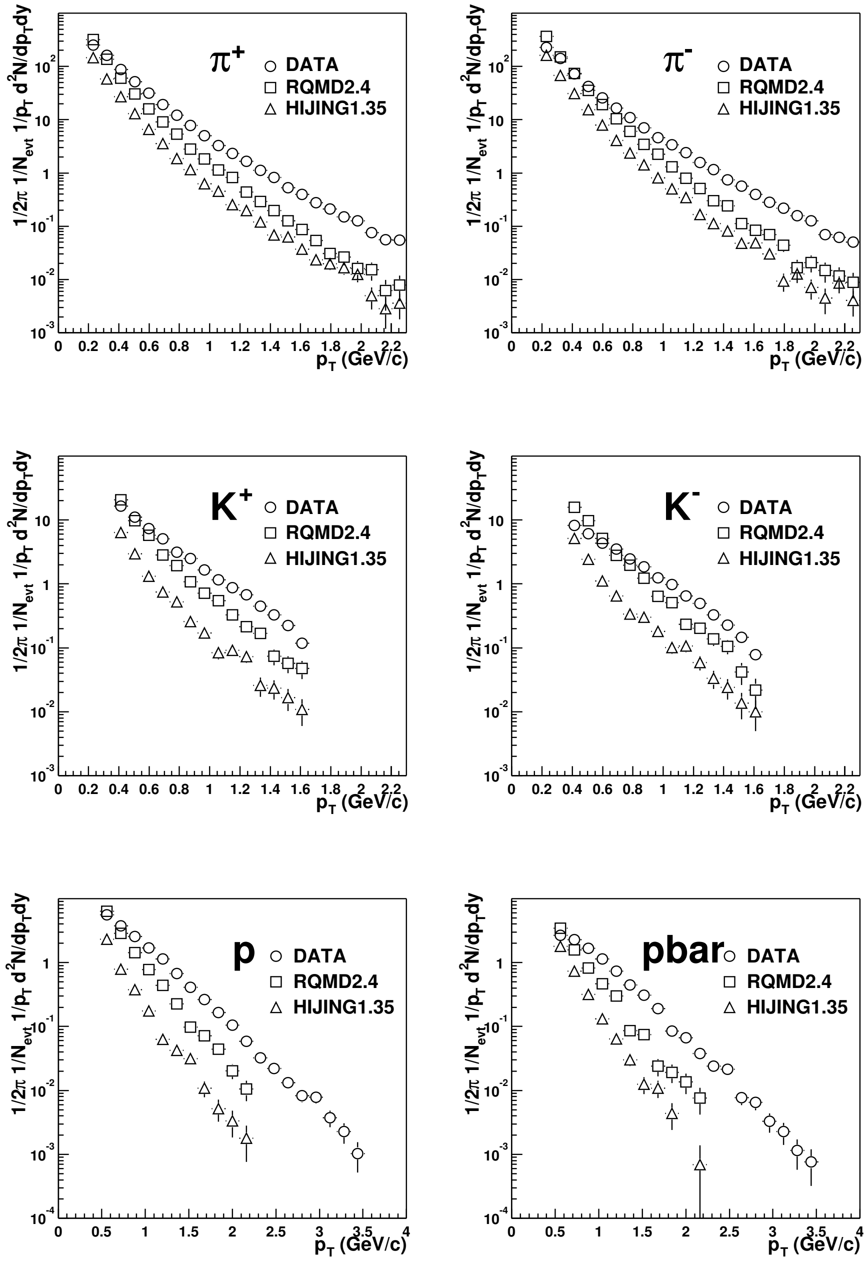

Figure 3.14: *Minimum bias p_T spectra for identified pions, kaons and protons shown together with simulated data (RQMD and HIJING).*

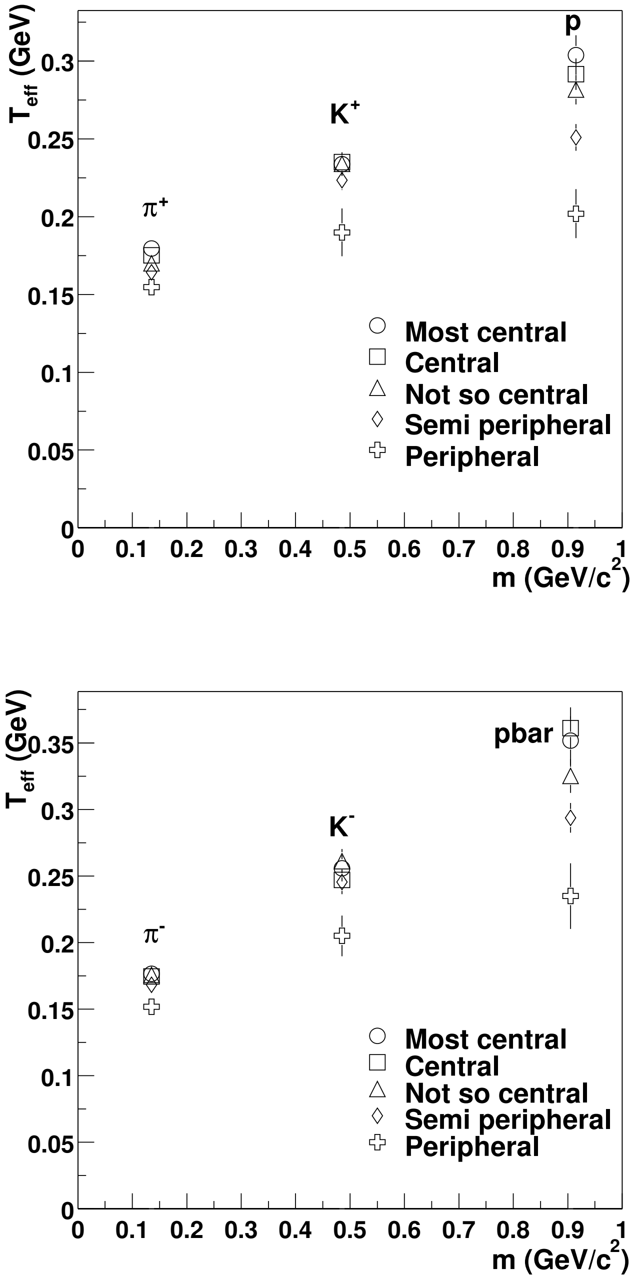

Figure 3.15: *Inverse slope parameters (T_{eff}) for positive and negative particles versus particle mass for five centrality classes.).*

Chapter 4

Pad Chambers in WA98 and PHENIX

An experience from the WA98 experiment was that space point tracking works excellently in a high multiplicity environment. A central event in WA98 had about 30-40 reconstructed tracks/m^2 at the first pad chamber, while in PHENIX there are about 16 tracks/m^2 in PC1.

4.1 Pad Chambers in the PHENIX experiment

If the chamber efficiencies are 100 % and the position resolution is good, three PC layers will suffice for space point tracking. If, on the other hand, the efficiencies are lower, three layers will not be enough. The measured efficiencies are above 99.5 % for all chambers, which is close enough. We also have maximal safety in each reconstructed point since we have many channels resulting in a low occupancy (2% in a central event) and clean data. A minimum of three fired neighbouring channels for each hit, make falsely reconstructed hits from noise highly improbable.

4.2 Pad Chambers in the WA98 experiment

The readout concept for the WA98 Pad Chambers was based on a custom-designed chip containing both analog and digital functions as well as ultra-thin mounting with the chip-on-board technique [42, 43, 44]. The detection efficiency of the chambers were in the range of 91-96%. Being Multi-Step Avalanche Chambers (MSAC:s), the anode pads are used to collect produced electrons. The pads, etched onto the circuit board backplane of the chamber, are read out with a moderate resolution of 6 bits, but due to the small cell size the achieved position resolution is very good (see Table 2.1 in chapter 2).

4.3 Pad layouts

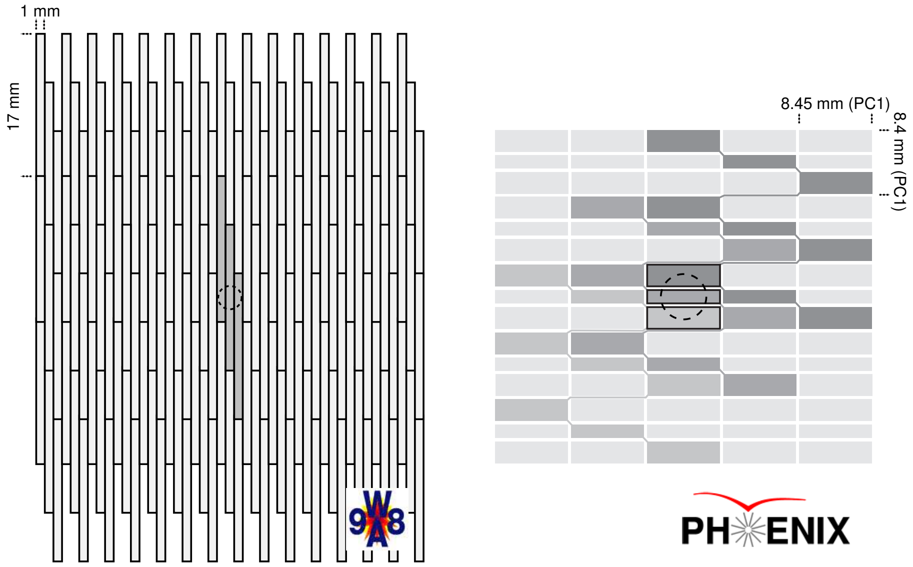

Figure 4.1: *Pad layout in the WA98 (left) and the PHENIX (right) Pad Chambers. The circles show the areas sensing the avalanche.*

The pad layouts in the WA98 and PHENIX Pad Chambers are shown in Fig. 4.1. In both cases, three neighbouring pads have fired. By staggering the pad pattern repeatedly by the period 3, the hits can be reconstructed with a factor 3 better resolution than the actual pad size.

A basic difference between the WA98 and PHENIX Pad Chambers is that the pads in WA98 were used to pick up the electrons released by the avalanche in the MSAC. In PHENIX, the pads sensed the fields of the drifting gas ions, released by the avalanche in the wire chamber.

4.4 Similarities

The very large number of channels, 72 000 for the WA98 Pad Chambers and 173 000 for the PHENIX Pad Chambers, where each channel represents a very small readout cell, is characteristic of the two solutions. The channel density makes it impossible to route all signals to the side of the detector, since multilayer boards are prohibited due to material constraints. The solution is to incorporate all functions in specially designed integrated circuits which are mounted on ultra-thin boards in multichip modules with the chip-on-board technique, and mount the electronics on the backplane, very close to the sensor pad.

A shared signal on three pads, reconstructed to an area 1/3 of the pad size, saves a factor 3 in the number of channels and makes the system totally immune against electronics noise.

The cost per channel could be kept low due to the simple nature of the information (1 bit per channel in the PHENIX PC) which also paid off in data volume, power budget, design complexity and simpleness of operation, all contributing to a very advantageous overall system cost. We can thus afford the many channels.

Chapter 5

The papers

Paper I: A large-acceptance spectrometer for tracking in a high multiplicity environment, based on space point measurements and high resolution time of flight

Nucl. Instr. and Methods A **431** (1999) 123-133.

A large acceptance tracking system, specially developed for tracking at very high particle densities encountered in ultra-relativistic heavy-ion collisions is described. The system is a combination of Multi-Step Avalanche Chambers equipped with electronic pad readout with high position resolution in two dimensions and streamer tube detectors, also with pad readout, with coarse position resolution, yet enough for safe pattern recognition. A high resolution time-of-flight system (time resolution better than 90 ps) provides particle identification up to 8 GeV/c for pions and pion/kaon separation up to 4 GeV/c. All detectors in the tracking system are read out with high performance integrated circuits. The system can operate at high event rates due to efficient zero suppression. The performance of the system for tracking under real running conditions with Pb-beam at 158 A GeV in the WA98 experiment at CERN is presented.

Paper II: The pixel readout system for the PHENIX pad chambers

Nuclear Physics A **661** (1999) 665c-668c.

A new concept for two-dimensional position readout of wire chambers is described. The basic idea is to use a cathode segmented into small pixels that are read out in specific groups (pads). The electronics is mounted on the outer face of the chamber with a chip-on-board technique, pushing the material thickness to a minimum. The system described here, containing 210,000 readout channels, will be used to read out the pad chambers in the PHENIX experiment at the Relativistic Heavy Ion Collider (RHIC).

Paper III: Event reconstruction in the PHENIX central arm spectrometers

Accepted for publication in Nucl. Instr. and Methods.

The central arm spectrometers for the PHENIX experiment at the Relativistic Heavy Ion Collider have been designed for the optimization of particle identification of particle identification in relativistic heavy ion collisions. The spectrometers present a challenging environment for event reconstruction due to a very high track multiplicity in a complicated, focusing, magnetic field. In order to meet this challenge, nine distinct detector types are integrated for charged particle tracking, momentum reconstruction, and particle identification. The techniques which have been developed for the task of event reconstruction are described.

Paper IV: Construction and performance of the PHENIX pad chambers

To be submitted to Nucl. Instr. and Methods.

We present the Pad Chamber detector system in the PHENIX experiment at the Relativistic Heavy Ion Collider, RHIC at Brookhaven National Laboratory. The three station system provides space points along each track in the spectrometer arms at midrapidity and covers a total area of 88 m^2. Its main function is to provide the track coordinate along the beam and to ensure safe pattern recognition at very high particle multiplicity. A new concept for two dimensional wire chamber readout via its finely segmented cathode was invented. The full readout system, comprising 172,800 electronic channels, is described together with the challenging design of the chambers. The electronics, mounted on the outer chamber face, together with the chamber itself amounts to 1% of a radiation length. Results from cosmic ray tests, showing an average efficiency better than 99.5% for all chambers are presented. The experiences from the full scale operation in the first run are reported.

Paper V: Centrality dependence of charged particle multiplicity in Au+Au collisions at $\sqrt{s_{NN}} = 130$ A GeV

Phys. Rev. Lett. **86** (2001) 3500-3505.

We present results for the charged-particle multiplicity distribution at midrapidity in Au-Au collisions at $\sqrt{s_{NN}} = 130$ A GeV measured with the PHENIX detector at RHIC. For the 5% most central collisions we find $dN_{ch}/d\eta_{|\eta=0} = 622 \pm 1(stat) \pm 41(syst)$. The results, analyzed as a function of centrality, show a steady rise of the particle density per participating nucleon with centrality.

Bibliography

[1] B. Schmidt et al., Astrophys. J. **507** (1998) L46-L63.

[2] A. Goobar et al., Physica Scripta **85** (2000) 47-58.

[3] S. Perlmutter et al., Nature **391** (1998) 51-54.

[4] G. Baym, Nucl. Phys. A **447** (1986) 463c.

[5] R. Brun et al., "PAW - Physics Analysis Workstation", CERN Program Library Long Writeup Q121. See also http://wwwinfo.cern.ch/asd/paw/.

[6] Rene Brun and Fons Rademakers, Proceedings AIHENP'96 Workshop, Lausanne, Sep. 1996, Nucl. Inst. and Meth. in Phys. Res. A 389 (1997) 81-86. See also http://root.cern.ch/.

[7] B. Nilsson-Almqvist and Evert Stenlund, Comp. Phys. Comm. **43** (1987) 387.

[8] H. Sorge, Phys. Rev. C **52** (1995) 3291.

[9] X. N. Wang and M. Gyulassy, Phys. Rev. D **44** (1991) 3501.

[10] H. J. Drescher et al., J. Phys. G: Nucl. Part. Phys. **25** No 10 (1999) L91.

[11] R. Brun and F. Carminati, "GEANT detector description and simulation tool", CERN Program Library Long Writeup W5013.

[12] D. Gross and E. Witten, Phys. Rev. D **21** (1980) 446.

[13] L. van Hove, Phys. Lett. B **118** (1982) 138.

[14] J.D. Bjorken, Phys. Rev. D **27** (1983) 140.

[15] J. Rafelski, Phys. Rep. **88** (1982) 331.

[16] J. Kogut and D. Sinclair, Phys. Rev. Lett. **60** (1988) 1250.

[17] T. Abbot et al., Phys. Rev. Lett. **64** (1990) 847.

[18] F. Antinori et al., Nucl. Phys. A **661** (1999) 130c-139c.

[19] T. Hatsuda and T. Kunihiro, Phys. Lett. B **185** (1987) 304.

[20] D. Lissauer and E. V. Shuryak, Phys. Lett. B **253** (1991) 15.

[21] J.-P. Blaizot and R. Mendez Galain, Phys. Lett. B **271** (1991) 32.

[22] S.V. Afanasev et al., Phys. Lett. B **491**, 59 (2000).

[23] M. M. Aggarwal et al., Phys. Rev. Lett. **85** (2000) 3595.

[24] T. Matsui and H. Satz, Phys. Lett. B **178** (1986) 416.

[25] C. Baglin et el. (NA38 collaboration), Phys. Lett. B **255** (1991) 459.

[26] J.-P. Blaizot and J.-Y. Ollitrault, Phys. Lett. B **217** (1989) 386.

[27] M. Gonin et al. (NA50 collaboration), Nucl. Phys. A **610** (1996) 404c.

[28] M.C. Abreu et al., Phys. Lett. B **410**, 327 (1997).

[29] M.C. Abreu et al., Phys. Lett. B **410**, 337 (1997).

[30] N. K. Glendenning, S. Pei and F. Weber, Phys. Rev. Lett **79** (1997) 1603

[31] A. Baden et al., Nucl. Instr. and Methods A **203** (1982) 189.

[32] W.T. Lin et al., Nucl. Instr. and Methods A **389** (1997) 415.

[33] H. Baumeister et al., Nucl. Instr. and Methods A **292** (1990) 81.

[34] R. Albrecht et al., Nucl. Instr. and Methods A **276** (1989) 131.

[35] M.M. Aggarwal et al., Nucl. Instr. and Methods A **372** (1996) 143.

[36] M.M. Aggarwal et al., Phys. Lett. B **420** (1998) 169.

[37] A. Breskin et al., Nucl. Instr. and Methods A **161** (1979) 19.

[38] A. Breskin et al., Nucl. Instr. and Methods A **178** (1980) 11.

[39] G. Charpak et al., Nucl. Instr. and Methods A **274** (1989) 275.

[40] M. Izycki et al., Nucl. Instr. and Methods A **310** (1991) 98.

[41] M.M. Aggarwal et al., Physics Letters B **477**, (2000) 37-44.

[42] L. Carlén et al., Nucl. Instr. and Methods A **391** (1997) 492.

[43] L. Carlén et al., Nucl. Instr. and Methods A **412** (1998) 361.

[44] L. Carlén et al., Nucl. Instr. and Methods A **413** (1998) 92.

[45] F. Retière, Ph.D. thesis, SUBATECH, Université de Nantes, Nantes, 2000.

[46] Phenix Collaboration, Conceptual Design Report (1993).

[47] D.P. Morrison, Nucl. Phys. A **638** (1998) 565c-569c.

[48] N. Saito, Nucl. Phys. A **638** (1998) 575c-578c.

[49] M.J. Bennett, Nucl. Phys. A **661** (1999) 661c-664c.

[50] K. Ikematsu et al., Nucl. Instr. and Methods A **411** (1998) 238.

[51] V.G. Riabov, Nucl. Instr. and Methods A **419** (1998) 363-369.

[52] Y. Akiba et al., Nucl. Instr. and Methods A **433** (1999) 143-148.

[53] Y. Akiba et al., Nucl. Instr. and Methods A **453** (2000) 279-283.

[54] M. Rosati, Nucl. Phys. A **661** (1999) 669c-672c.

[55] G. David, IEEE Trans. Nucl. Sci. Vol.43 No.3 (1996) .

[56] L. Carlén et al., Nucl. Instr. and Methods A **396** (1997) 310-319.

[57] I.G. Bearden et al., Phys. Rev. Lett **78** (1997) 2080.

[58] G. Roland et al., Nucl. Phys. A **638** (1998) 91c-102c.

[59] C.A. Ogilvie et al., Nucl. Phys. A **638** (1998) 57c-68c.